



Solar heat localization: concept and emerging applications

Journal:	<i>Journal of Materials Chemistry A</i>
Manuscript ID	TA-REV-01-2020-001004.R1
Article Type:	Review Article
Date Submitted by the Author:	10-Mar-2020
Complete List of Authors:	Kashyap, Varun ; University of Houston System, Mechanical Engineering Ghasemi, Hadi; University of Houston System, Mechanical Engineering

SCHOLARONE™
Manuscripts

Journal of Mat Chem A

REVIEW ARTICLE

Solar heat localization: concept and emerging applications

Varun Kashyap,^a and Hadi Ghasemi^{*a}

Received 00th January 20xx,
Accepted 00th January 20xx

DOI: 10.1039/x0xx00000x

Recently, solar heat localization concept has provided an appealing route for efficient utilization of solar thermal energy. This concept has shown remarkable promise in power generation, desalination, distillation, water splitting, sterilization, oil spill cleanup, electricity generation from salinity and also CO₂ capture. In this concept, a material paradigm localizes the solar irradiation forming a hot spot in the material and minimizes the energy losses to the surrounding environment. In most applications, the localized thermal energy is used for liquid-vapor phase change in which the material wicks the liquid into the hot spot to generate hot steam. In contrast to conventional steam generation systems, thermal losses are reduced significantly, thereby offering high evaporation efficiencies. In this comprehensive review, physics of solar heat localization is elaborated and a roadmap on necessary material properties is provided to achieve superior performance through this concept. The current advancements on synthesis of new materials for solar heat localization are discussed in detail. Various applications of this concept are explored individually and the figures of merit for each application are elucidated. A comparative analysis is conducted for these figures of merit on a wide range of studies and key takeaways are highlighted. Finally, the current challenges and future prospects for technological implementation of this concept are reviewed. As solar energy is the most abundant renewable energy resource on earth, this concept could open a path to significantly reduce carbon foot print of electricity and water generation in the world.

1. Introduction

Evaporation is a fundamental and pervasive phenomenon in nature which envelops a range of technologies and principles which guard our very existence. It is critical for water cycle which is a pivotal cycle operated by nature. Power generation, electronic cooling, food processing, health, desalination and sterilization are only a few domains where the phenomenon of evaporation has a wide footprint. However, evaporation for such applications is still an energy intensive process due to high phase-change enthalpy. Recently, interest towards studies using renewable sources of energy has been tested to reduce or eliminate the use of fossil fuels¹. Among various forms of renewable energy sources available, solar energy is one of the most abundantly available resource on earth as shown in Fig 1a²⁻⁶. Use of solar irradiation to power energy intensive evaporation processes is an attractive approach since the hourly incident solar flux on the surface of the earth is greater than the annual global energy consumption⁴. Solar-thermal energy has been used to power various above mentioned systems in previous studies⁷⁻¹⁰. However, most current systems suffer from high optical and surface losses. They use

concentrators and intermittent mediums to transfer energy to the bulk fluids¹¹⁻¹⁹. In addition, the bulk fluid is in thermal equilibrium with the generated steam which leads to low evaporation efficiency in these systems. The evaporation efficiency is defined as the ratio of the thermal energy stored in the vapor generated to the total incoming solar flux and can be written as

$$\eta = \frac{\dot{m}h_{LV}}{C_{opt}q_i} \quad (1)$$

Where \dot{m} denotes the mass flux, h_{LV} the total enthalpy of liquid vapor transformation (i.e. sensible heat + phase-change enthalpy), C_{opt} the optical concentration and q_i the nominal direct solar irradiation 1 kWm⁻². As the sensible heat is much smaller than enthalpy of phase change, the evaporation efficiency is an approximately linear function of \dot{m} . The vapor and liquid temperatures affect the sensible heat and the enthalpy of phase-change in h_{LV} calculations and thus need to be accurately measured. Following the above equation, several methods and material paradigms have been proposed to reach high thermal efficiencies at nominal solar irradiation. This has been achieved due to accelerated study in the domain of solar driven interface evaporation. Neumann et al.²⁰ succeeded in generating steam with Au nanoparticles using volumetric heating. This work laid the foundation for systems where solar based direct steam generation can be induced without heating the bulk liquid to the boiling point. However, requirement of

^a Department of Mechanical Engineering, University of Houston, 4726 Calhoun Road, Houston, Texas 77204-4006, USA

† Footnotes relating to the title and/or authors should appear here.

Electronic Supplementary Information (ESI) available: [details of any supplementary information available should be included here]. See DOI: 10.1039/x0xx00000x

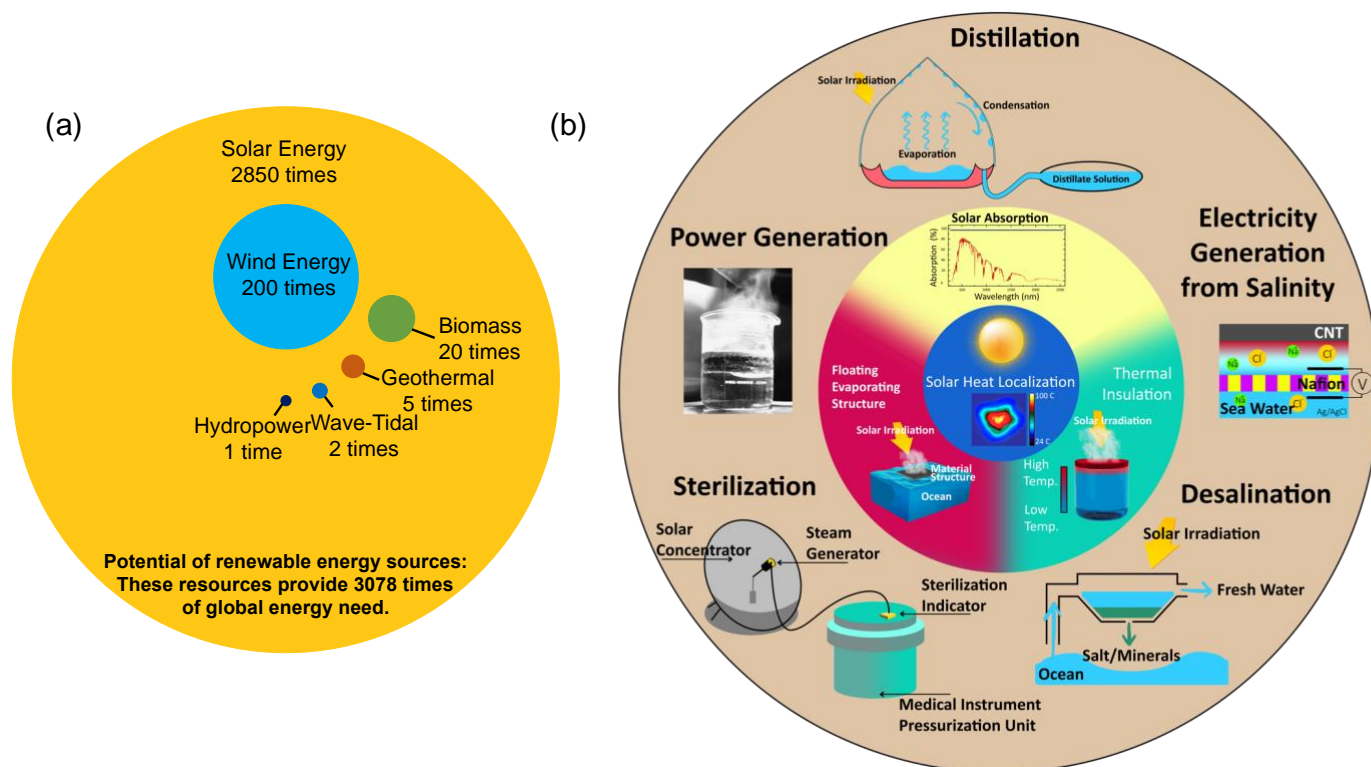


Figure 1 Solar heat localization approach. (a) Solar energy is abundantly available on the earth's surface and has order of magnitude higher potential compared to other renewable resources. (b) Material system for solar heat localization consists of three main components including a solar absorber, floating evaporation structure and thermal insulation. Prominent applications of solar heat localization are highlighted.

large optical concentrations (103 kWm^{-2}) and their low solar thermal conversion efficiency (24%) limited their usage. Subsequently, Ghasemi et al.²¹ proposed the concept of solar heat localization for steam generation and developed a Double Layered Structure (DLS) to demonstrate the principle. This study provided a platform for solar steam generation at low optical concentrations. A floating structure of a carbon-based material (Exfoliated graphite) was used as the light absorber to convert the incident light into heat. The heat was localized at the material interface, thereby creating a hot spot. Water pathways facilitated the transport of water to the interface through capillary forces. Steam was generated while the underlying water remained at ambient temperature. Therefore, by minimizing heat losses, an efficiency of 85 % was obtained at 10 kWm^{-2} . Subsequently, a range of materials have been explored towards highly efficient solar steam generation including polypyrrole (PPy) and plasmonic films, titanium nitride, silicon nanoparticles, rGO, functionalized graphene, graphene aerogels, magnetic particles, natural mushroom and carbonized rayon. Several other technologies and material structures have been studied towards enhanced steam generation at ambient conditions. G. Ni et al.²² succeeded in generating steam under 1 kWm^{-2} (one sun) through thermal localization. Cooper et al.²³ developed an approach for superheated steam generation under one sun solar irradiation. The concept of solar driven interface evaporation has found numerous applications in various domains including desalination, sterilization, water

purification, water splitting, oil clean up and CO₂ capture and conversion to name a few as shown in Fig. 1b. Recent studies have also shown interest in the cost analysis of these technologies for large scale implementation.

In this review, the concept of solar heat localization has been elaborated along with broad material classifications, and designs to implement this concept. Their solar thermal efficiencies under various optical concentrations and improvement strategies have also been discussed. Furthermore, the concept of heat localization utilized for various above-mentioned ground-breaking applications have been analysed and finally scalability of viable materials and technologies for large scale implementation have been discussed. This wholistic review provides a detailed understanding of factors for material design and key figures of merit for applications of solar interface evaporation technology studies.

2. Concept

In conventional methods of solar energy harvesting, the generated steam is in thermal equilibrium with the bulk liquid. The incident solar radiation is absorbed by a cavity and the heat is transferred to the bulk liquid using an intermittent medium. These systems have inherent thermal losses associated with them which leads to low evaporation efficiencies. Furthermore,

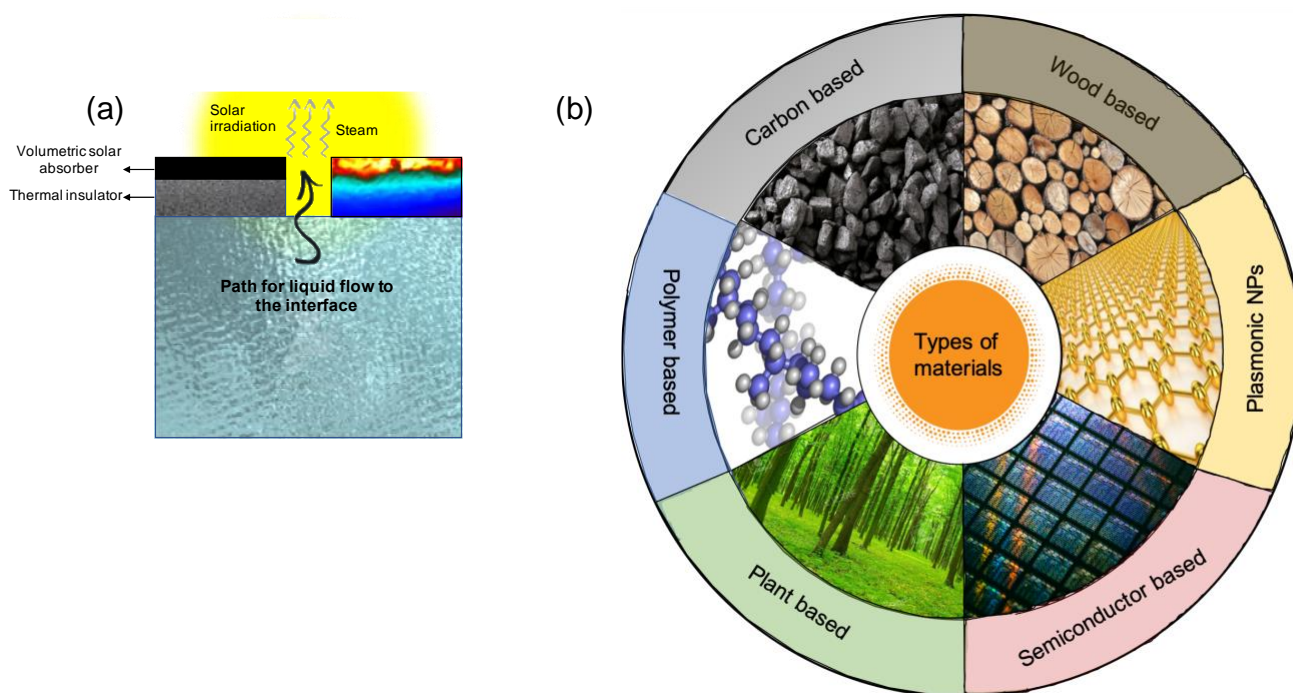


Figure 2 Types of materials and figures of merit. Desired properties in these materials and their broad classification are shown. (a) Figures of merit for a material used in solar heat localization are illustrated. Tuning these properties is critical for enhanced performance of these materials for various applications. (b) Broad classification of materials used for heat localization are shown. The choice of these materials is based on the desired material properties.

since the ambient solar flux (1000 W m^{-2}) does not provide enough power per unit area of the absorber to reach high surface temperatures, optical concentrators are used which contribute to cost intensive nature of these systems. In the new concept of solar heat localization, as shown in Fig. 2a, a material structure which is buoyant at the liquid surface and has high volumetric absorption in the solar spectrum localizes the heat at the liquid-vapor interface, thereby creating a hot spot. Due to low thermal conductivity of the material structure, the bulk liquid underneath is maintained at ambient temperature. The liquid wicks to the hotspot by capillary force and evaporation takes place at the interface. This approach reduces thermal losses significantly including conductive losses to the underlying liquid, thereby increasing the evaporation efficiency significantly. Also, since all the heat is localized at the liquid-vapor interface, higher surface temperatures can be achieved at lower solar concentrations. This opens a path for high efficiency solar thermal energy harvesting for various applications including power generation, desalination, distillation, sterilization and CO_2 capture. For desalination, in addition to the above-mentioned properties, a mechanism is required to prevent salt accumulation on the material structure to ensure long term operation. These mechanisms are discussed in a later section. In other applications such as CO_2 capture, the concept of heat localization is used to stimulate solid-liquid phase change. The material structure concentrates the solar irradiation required for phase change while minimizing energy losses.

3. Materials

3.1. Material properties

The important characteristics in a material for evaporation at the liquid-vapor interface using the concept of heat localization are (a) high volumetric absorption in the solar spectrum, (b) low thermal conductivity, (c) buoyant at the liquid surface, and (d) continuous fluid transport to the liquid vapor interface. Several studies have focused on improving these characteristics of the material paradigm. The above characteristics of materials can be further classified into two types, (i) thermal and optical properties, (ii) fluid transport properties based on hydrodynamics of flow. **Table 1** shows the summary of thermal and optical properties of various materials from several works.

3.1.1 Absorption in the solar spectrum

Efficient absorption in the solar spectrum is an important property for a material used for solar heat localization. The solar spectrum spans from around 300 nm to 2500 nm. The chosen material needs to absorb effectively in this range of wavelengths, thereby having minimum reflective and transmission losses. Two main categories of solar absorbers include carbon-based materials and plasmonic materials. Direct use of carbon-based materials or carbonization of other materials enhances their solar absorption. This occurs due to

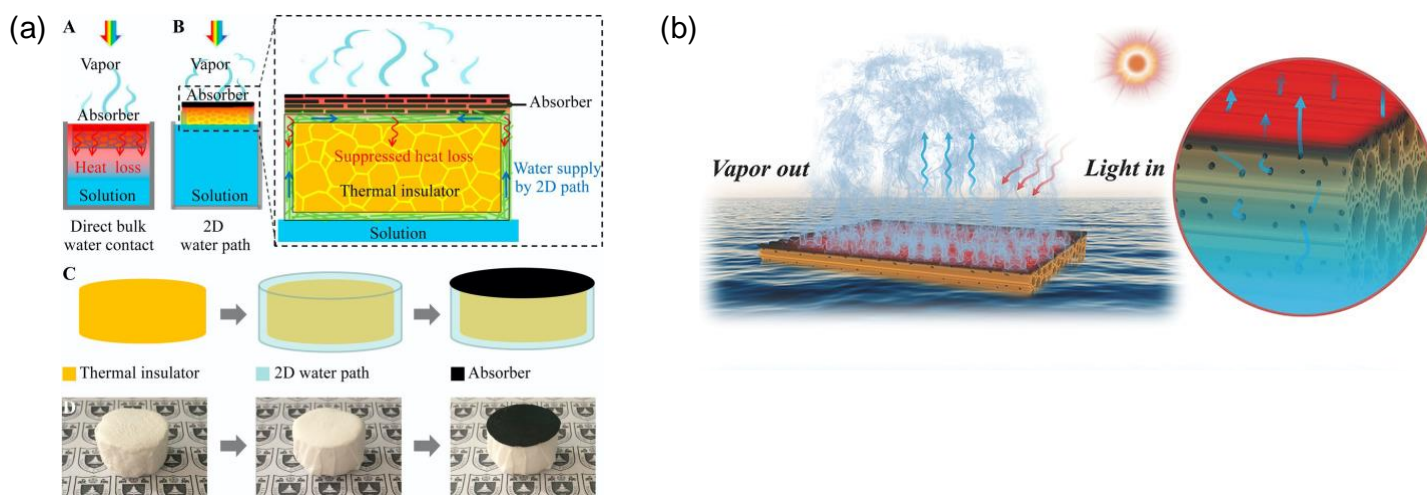


Figure 3 Dynamics of liquid flow to the interface. Different types of transport mechanisms for continuous liquid delivery to the liquid-vapor interface are shown. (a) In this approach, the absorber is separated from the bulk water by a thermal insulator and a 2D pathway is enabled with a thin layer of cellulose wrapped around the insulator. (b) Here, 3D pathways are used which are present in horizontal porous wood. Its interconnected porous structure enables efficient liquid transport to the liquid-vapor interface. Ref: Xiuqiang Li et al²⁵¹ & Liu et al³⁷.

excitation of electrons and their subsequent relaxation²⁴. In addition to having high absorption in the solar spectrum, low thermal emittance is required in order to suppress the radiative losses due to high surface temperatures. Ghasemi et al.²¹ used exfoliated graphite as their solar absorber which has ~97% absorption in the solar spectrum. Several other works have developed material structures to have these desired properties as shown in Table-1. In the case of plasmonic nanoparticles, they only absorb a narrow band of wavelengths around their resonance peak. In order to have a broad range of absorption, several works including Zhou et al.²⁵, used closely packed nanoparticles with a range of sizes assembled in a nanoporous structure. By doing so, there is an overlap of the plasmon resonance modes leading to broadband absorption. Solar absorption of ~99% was obtained using plasmonic nanoparticles. This is discussed in detail in a later section.

3.1.2 Thermal conductivity

Tuning the thermal conductivity of the material structure is critical for two reasons, (i) to localize the heat at the liquid-vapor interface. (ii) prevent heat loss to the underlying liquid and thereby improve the evaporation efficiency. Table 1 shows the thermal conductivities of materials used in various works. Carbon based materials and polymeric materials show extremely low thermal conductivities and are popular choices to obtain this property in the material structure. A single carbon layer (e.g. exfoliated graphite) results in increased conductive losses to the underlying liquid. In order to prevent these losses, Ghasemi et al.²¹ used a second insulating layer of carbon foam underneath. Subsequently, several composite materials were developed where a polymer matrix was used to hold the carbon material in a single material structure^{26,27}. Other materials including wood and polystyrene foams have been used in both single layered and multilayered structures. Another class of

materials used for this purpose are aerogels. Graphene aerogel has shown to have high solar absorption in addition to low thermal conductivity and therefore is a popular choice.

3.1.3 Buoyancy at the liquid surface

In order to ensure interfacial heating and evaporation, the material structure needs to float at the liquid-vapor interface. This has been achieved by tuning density and porosity of the materials used. Several materials have been used for this purpose including, carbon foams, air-laid paper, AAO membrane, PDMS and liquid latex. Although most works have used a floating material structure for solar heat localization, it is not a primary requirement for this purpose. Localized heating is also achieved in solution-based system by dispersing large concentrations of nanoparticles in them. Solar absorption takes place within a thin layer close to the liquid-vapor interface. An essential parameter for interfacial evaporation is the mechanism of flow of liquid to the heat localized surface or the hot spot. Although several works and review articles have spoken about thermal and optical properties, the importance of hydrodynamics of flow has not been elaborated in detail. In this work, we provide the physics for the optimal design of materials for continuous fluid transport to the liquid-vapor interface in different types of material structures and their importance in developing better technologies for various applications in the following section.

3.1.4 Hydrodynamics of fluid flow to the interface

An important criterion for high evaporation rate and subsequently high efficiency in solar interfacial evaporation is to ensure continuous liquid transport to the heat localized region or the hot spot. For this purpose, most works on interfacial evaporation have used highly porous material to facilitate fluid transport to the liquid-vapor interface by capillary

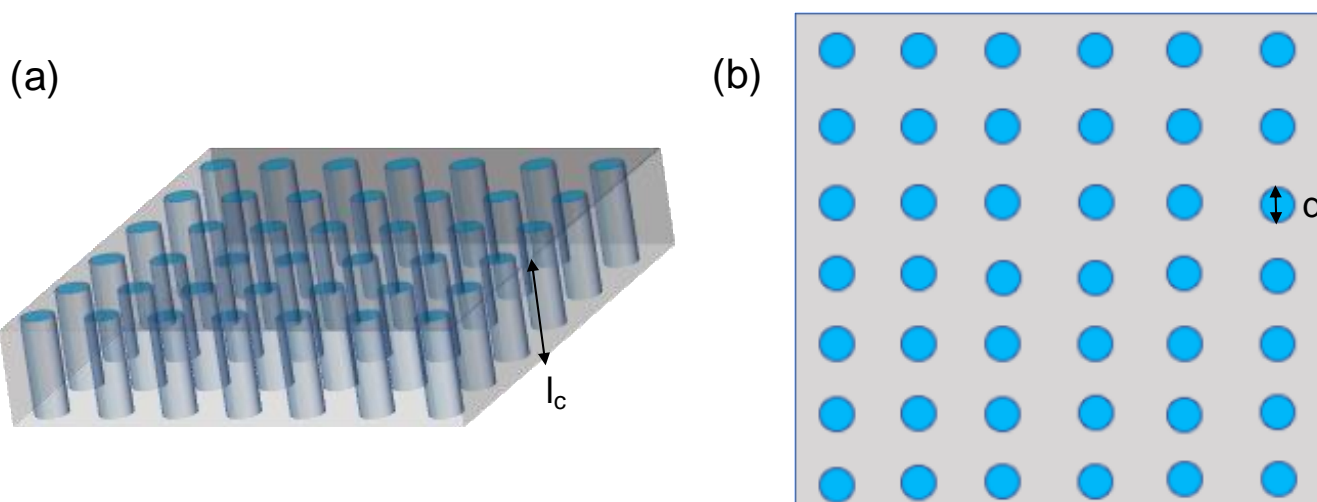


Figure 4 Assumption of a porous structure. A porous structure is assumed to be an array of cylindrical conduits to calculate the flow rate for wicking. (a) & (b) Different views for the porous structure that enables liquid transport to the liquid-vapor interface is shown. Regularly placed cylindrical pores are assumed. The diameters and capillary lengths of these pores are indicated in the figure.

force. In this section, we discuss the physics or hydrodynamics of flow in porous structures, the liquid flow on rough surfaces and the governing equations for this type of capillary flow. In addition, various mechanisms used in literature are also elaborated.

The force required for the liquid to flow through a capillary tube is given by the young's relation which is $\gamma_{SV} - \gamma_{SL} = \gamma \cos \theta$, where γ_{SV} and γ_{SL} are the solid/liquid and solid/vapor surface energies, γ is the liquid/vapor surface tension and θ is the contact angle of the liquid on the solid. Therefore, in this case (for wicking), the driving force is the surface tension force which is balanced by the weight of the liquid column. In case one, neglecting gravity, we can balance the constant driving force (of the order of γa , where a is the tube radius) with the viscous friction force ($\mu V z$, where V is the velocity of the meniscus, z is the position and μ is the liquid viscosity)²⁸. Thus, we find the Washburn law, which states that the position of the meniscus increases as the square root of time, $z \sim (Dt)^{1/2}$, where D is the dynamic coefficient given by $D \sim \gamma a / \eta$. However, the Washburn law only accounts for a single geometrical parameter (radius, a) and therefore cannot be used directly for rough surfaces. This is discussed in a later section. In case two, in order to consider the effect of gravity, it is important to define a criteria. The gravitational effect is negligible compared to the surface tension when $a < l_c = [\gamma / (\rho g)]^{1/2}$, where l_c is the capillary length and ρ is the liquid density. When this condition holds good, the surface tension dominates and the liquid wicks through the porous surface. Porous surfaces have an inherent advantage over other smoother surfaces since porous hydrophilic surfaces can absorb significantly higher amounts of liquid as compared to smooth surfaces against gravity. Interestingly, Seong Jin Kim et al.²⁹ also observed that although the capillary forces dominate in a hydrophilic porous substrate, flooding occurs

when the flow rate exceeds a threshold value. Therefore, it is important to determine this threshold flow rate for a porous material. In order to do this, Seong Jin Kim et al. studied the dynamics of wicking into hydrophilic porous media from an infinite point source. The radius of the liquid blot on porous surface follows the Darcy law:

$$\dot{R}_w = \frac{Q_w}{\phi A_c} \sim \frac{\kappa}{\phi \mu} \frac{\Delta P}{R_w} \quad (2)$$

Where the dot represents the time derivative, Q_w is the wicking flow rate, A_c is the area of the wet front perpendicular to the fabric plane of thickness c ($= 2\pi c R_w$), κ is the in-plane permeability of the porous medium and ϕ is the porosity. The pressure drop at the liquid-gas interface within the porous medium can be given by the Young Laplace equation given by $\Delta P = 2\gamma \cos \theta / r$. As shown in Fig. 4, the assumption followed is that the fabric of the porous structure is a regular array of cylindrical conduits with hydraulic radius, r . Hydraulic radius, r is a function of ϕ and fiber radius r_f and is defined as $r = r_f \phi / (1 - \phi)$. Integrating equation (2) with respect to time t ,

$$R_w \sim 2 \left[\frac{\kappa (1 - \phi) \gamma}{r_f \phi^2 \mu} t \right]^{1/2} \quad (3)$$

The propagation of the wetting front follows the Washburn rule and therefore, the flow rate of wicking, Q_w can be written as

$$Q_w \sim 4\pi \frac{c \kappa (1 - \phi) \gamma}{r_f \phi \mu} \quad (4)$$

According to the above equation, the flow rate is a function of fabric properties ($c \kappa (1 - \phi) / r_f \phi$) and the liquid property (γ / μ). Therefore, in the case of fluid flow to the liquid/vapor interface for interfacial evaporation, since the liquid properties are constant for water, the fabric or porous material properties

can be tuned based on the above relation for higher flow rate to the interface. However, note that Q_w is regarded as the maximum flow rate from a point source that can be absorbed by a porous medium and hence can be directly related to the evaporation rate.

The hydrodynamics of flow changes when the fluid wicks through hydrophilic rough surfaces. This behavior is termed as hemiwicking. For wicking on rough surfaces, a single geometric parameter (radius) cannot be used to describe the hydrodynamics of flow as described earlier. For example, a square array of circular micropillars requires three parameters including the height, diameter and spacing of the pillars. Therefore, for the appropriate correction in the Washburn equation, different dynamic coefficients have been suggested by various works^{28,30–33}. However, these studies involve regularly spaced micropillar arrays. A more general study on the dynamics of hemiwicking is provided by Jungchul Kim et al.³⁴. They define a scaling law at macroscopic length scales which is independent of the precise arrangement of micropillars. They prove that the distance from the reservoir to the wicking front L , grows as a function of $(\eta\gamma h/\mu)^{1/2}t^{1/2}$ where η is a generalized co-efficient defined in terms of the dimensions of pillar array, $(\eta = (f - 1)/[1 + h(f - 1)/s])$ where h is the height of the pillars, f is the roughness defined as the ratio of solid surface area to the projected area, and s is defined based on the diameter of the pillars, d and transverse pitch, s_y as $s = s_y - d$. However, it can be further challenging to predict hydrodynamics of flow for randomized rough surfaces.

New approaches have been studied by various groups for 1D, 2D and 3D water pathways to improve fluid flow to the interface for enhanced evaporation as shown in Fig. 3. Xiuqiang Li et al.³⁵ developed an angular absorber to which water was transported by 1D pathway. By doing so, they reported an evaporation efficiency of 85%. In another interesting work, also by Xiuqiang Li et al.³⁶, 2D water pathway was developed which consisted of a 2D cylindrical surface wrapped on polystyrene foam having an extremely low thermal conductivity of $0.04 \text{ Wm}^{-1}\text{K}^{-1}$. Hydrophilic cellulose was wrapped around the surface of the thermal insulator, thereby providing a 2D path for the liquid that is circulated by capillary forces. Note that the common feature of both these studies is the separation of the thermal insulator from the liquid transport structure. The pores of the insulator are designed to be closed to provide enhanced thermal insulation whereas the pores of the liquid transport structure remains open for continuous fluid transport to the interface. In another study by He Liu et al.³⁷, a reverse tree design was implemented which consists of a naturally formed 3D interconnected micro/nanochannels for fluid transport. This coupled with extremely low thermal conductivity ($0.11 \text{ Wm}^{-1}\text{K}^{-1}$) provides an efficiency of 89% at 10 sun solar concentration. In this way, several approaches are being considered for better fluid transport to the interface which is a critical material

property to be considered for improved performance. Understanding the hydrodynamics of fluid transport is critical for design of these materials for various applications.

3.2 Types of materials

The materials used for heat localization have been broadly classified into the following categories: carbon based, plasmonic based, wood based, plant based and polymeric materials as shown in Fig. 2b. In addition to these, other materials have been utilized in various studies to develop composite structures having the aforementioned properties for enhanced performance. Few of these materials and related studies are discussed in these sections along with their material properties.

3.2.1 Carbon based materials

Carbon is a very convenient choice for a solar absorber since it is naturally black and also has significant absorption in the solar spectrum. Although these carbon-based materials are excellent solar absorbers, additional modifications maybe required for better thermal insulation and mechanisms for liquid supply to the solar absorber. Several polymeric materials, networked matrices and foam structures have been used for this purpose which are discussed in a later section. Among various carbon-based materials studied, graphene, carbon nano tubes (CNTs), reduced graphene oxide (rGO), carbon black and carbon spheres are popular choices. Graphene is a promising candidate as a solar absorber for solar steam generation due to its outstanding photon-harvesting ability and tunable thermal conductivity by chemical doping. However, due to its inherent hydrophobic property, graphene is not used as a standalone component for this application³⁸. Therefore in a work by Ito et al.³⁹, porous graphene was functionalized either by nitrogen doping or by using hydrophilic groups, thereby making it more suitable for this application. This porous graphene also serves as a channel for liquid transport and achieves a high solar thermal efficiency of 80% with an evaporation rate of $1.5 \text{ kgm}^{-2}\text{h}^{-1}$ under 1 sun solar illumination. The surface temperature of porous graphene sheets in this study reached a temperature as high as $105 \text{ }^\circ\text{C}$ at this solar concentration within 2 minutes. In another approach by G. Ni et al.¹⁸, graphene was used which was dispersed in water for solar vapor generation. The advantage of this work was that carbon-based nanoparticles have better broadband solar absorptance compared to metal nanoparticle suspensions and also cost significantly less. Solar thermal efficiency of 69% was obtained under 10 sun solar concentration while achieving surface temperatures $> 80 \text{ }^\circ\text{C}$. In another approach, graphene oxide aerogels were used as solar absorbers⁴⁰. With excellent absorption in the solar spectrum ($>92\%$) and high porosity and extremely low thermal conductivity ($>0.05 \text{ Wm}^{-1}\text{K}^{-1}$), they serve as excellent candidates for solar steam generation. A solar thermal efficiency of 83% was obtained under 1 sun solar concentration with $1.6 \text{ kgm}^{-2}\text{h}^{-1}$ evaporation rate. Carbon nanotubes (CNTs) are popularly used as solar absorbers. CNT layer being hydrophobic, it is coupled with a hydrophilic layer for improved fluid transport to the heated surface of the absorber (CNTs). In a work by Yuchao Wang et

al.⁴¹, CNT is used as the top layer and macroporous silica is used as the bottom substrate. Surface temperatures as high as 70 °C was

Table 1: Material properties

Type of material	Abs (%)	WL range (nm)	Therm cond (Wm ⁻¹ K ⁻¹)	Reference
Carbon based materials				
Black PAN/CB membrane on green leaf	97	400-2500	-	⁴² Shendong Zhuang et al.
Modified graphene aerogel	94	300-1500	0.15	⁴³ Yang Fu et al.
Activated carbon fiber felt	94	400-2500	0.43	⁴⁴ Haoran Li et al.
Black titania/graphene oxide nanocomposite film affixed to airlaid paper, polyethelene foam	90	400-2500	0.04	⁴⁵ Xinghang Liu et al.
Carbon particles on the air-laid paper (C-paper)	98	200-1200	0.44	⁴⁶ Shang Liu et al.
Graphite nonwoven film	98	250-2500	-	⁴⁷ Xiuqiang Li et al.
Reduced graphene oxide and silk fabric	90, 94	350-1000, 1000-2500	-	⁴⁸ Qian Zhang et al.
Graphite powder (GP) and a semipermeable collodion membrane (SCM)	97.8	200-1100	-	⁴⁹ Fujun Tao et al.
Crumpled graphene balls	97.4	350-2500	0.032	⁵⁰ Wei Hao et al.
Monolithic carbon-aerogel	99	400-2500	0.19	⁵¹ Peng Mu et al.
Carbonized moldy bread	96	300-1300	0.42	⁵² Yaoxin Zhang et al.
Superhydrophobic carbon black (CB) nanoparticles	92.92	400-2500	-	⁵³ Miaomiao Ye et al.
Patterned surfaces by printing carbon black on the air-laid paper	~80	250-2500	0.03	⁵⁴ Yini Luo et al.
Graphene Aerogel	92	400-2500	0.05	⁵⁵ Xiaozhen Hu et al.
3D Printed CNT-GO and CNT-NFC	~97	400-2500	0.04	⁵⁶ Yiju Li et al.
Carbon Nanotube Membrane on Macroporous Silica Substrate	~97	200-800	0.2	⁴¹ Yuchao Wang et al.
Carbon nanotube nanofluid	~90	400-800	-	⁵⁷ Xinzhi Wang et al.
rGO/mixed cellulose esters	95	500-2500	0.56	⁵⁸ Gang Wang et al.
rGO polyurathene nanocomposite foam	91	300-1500	0.51	⁵⁹ Gang Wang et al.

rGO with polystyrene foam	~96	300-800	0.03	⁶⁰ Le Shi et al.
Nitrogen-doped graphene/carbon hybrid aerogel (NGCA) using graphene oxide (GO) and melamine form (MF)	97.57	200-2500	0.39	⁶¹ Bingbing Huo et al.
Plasmonic materials				
Nanoporous gold nanoparticle (AuNP)/poly(p-phenylene benzobisoxazole) nanofibre (PBONF) composite films	67.4	300-2500	0.23	⁶² Meiling Chen et al.
Ag@TiO ₂ nanoparticles	-	-	0.48	⁶³ Haoran Li et al.
Au@TiO ₂ core-shell nanoparticles	~70	400-2000	-	⁶⁴ Jian Huang et al.
C-Au-TiO ₂	75	600-2500	-	⁶⁵ Jian Huang et al.
Plasmonic covellite CuS hierarchical nanostructure	~90	200-1100	-	⁶⁶ Fujun Tao et al.
Gold nanospheres and nanostars are assembled into ridges/disordered nanohole arrays	90	200-2500	-	⁶⁷ Guofen Song et al.
Cu nanoparticles within the carbon decorated oxygen-vacancy-rich TiO ₂ matrix	~92	400-2500	-	⁶⁸ Xiangcheng Zhang et al.
Copper mesh, graphadiyne, CuO nanowires	86	400-1500	-	⁶⁹ Xin Gao et al.
Au nanoparticles with airlaid paper supporting layer	87	400-2500	0.3	⁷⁰ Yanming Liu et al.
Self-assembly of metallic nanoparticles onto a nanoporous template	99	400-2500	-	²⁵ Lin Zhou et al.
Plasmonic nanoparticles (Au/NPT)	90	550-2500	-	⁷¹ Lin Zhou et al.
Nanolayers of Reusable Biomimetic Nanoparticles	97	350-1450	-	⁷² Changxu Liu et al.
Flexible thin-film black gold membranes	91	400-2500	-	⁷³ Kyuyoung Bae et al.
Cotton, photothermal CuS yolk-shell nanocages and agarose aerogel	93	290-1400	0.04	⁷⁴ Xuan Wu et al.
Hydrophobic Fe ₃ O ₄ @C core-shell nanostructures	90.3	350-2500	-	⁷⁵ Rong Chen et al.
CuS nanoflowers and semipermeable collodion membrane (SCM)	~96	200-1100	-	⁷⁶ Fujun Tao et al.

Tungsten carbide (WC) nanoarray film	97.5	220-2200	-	⁷⁷ Nana Han et al.
Wood based materials				
Wood-polydopamine	97 (no transmission losses included)	200-800	0.13	⁷⁸ Xuan Wu et al.
Bi-layer system (C-wood)	98	400-2500	0.4	⁷⁹ Xiao Luo et al.
Wood graphene oxide composite	-	-	0.53	⁸⁰ Keng-Ku Liu et al.
F-Wood/CNTs membrane	98	300-1200	0.21	⁸¹ Chaoji Chen et al.
Flame treated wood	99	400-2500	0.33	⁸² Guobin Xue et al.
Different natural woods	96	250-2500	0.34	⁸³ Chao Jia et al.
Flexible porphyrin organic framework	95	300-1300	-	⁸⁴ Zi-Jing Xia et al.
Plant based materials				
Coating a thin layer of carbon nanotubes (CNTs) on the top surface of a tree stump with roots	~95	300-1200	-	⁸⁵ Yilin Wang et al.
Carbonized lotus seedpods	98	250-2000	0.04	⁸⁶ Jing Fang et al.
Reduced graphene oxide wrapped plant fiber sponges (PFS@rGO)	95.5	200-1400	0.4	⁸⁷ Tingjie Chen et al.
Surface-carbonized de-sugaring stems of sugarcane	98.4, 95	300-780, 780-2500	0.22	⁸⁸ Jie Liu et al.
Natural and carbonized mashroom, carb mash	96	400-2500	0.04	⁸⁹ Ning Xu et al.
Polymer based materials				
Polypyrrole (PPy) coated cotton fabric	90	200-2600	0.52	⁹⁰ Dandan Hao et al.
PPy-coated membranes	94	400-2500	0.02	⁹¹ Canzhu Wang et al.
Surface modified polyurethane (PU) sponge	~80	400-2500	0.14	⁹² Zheng Zhang et al.
Kapok fibers-PPy aerogels	97	200-2000	0.02	⁹³ Peng Mu et al.
Polypyrrole (PPy) wood	97.5	250-2500	0.5	⁹⁴ Wei Huang et al.
Artificial mashroom made of the common poly- vinyl alcohol sponge coated with charcoal,	98	400-2500	0.46	⁹⁵ Xiujun Gao et al.
Conjugated microporous polymer (CMP) aerogel	-	-	0.022	⁹⁶ Peng Mu et al.

Double-network hydrogel with a porous structure (p-PEGDA–PANI)	98.5	400-2500	0.43	⁹⁷ Xiangyu Yin et al.
PEGylated MoS ₂ -cotton cloth	90	200-2000	-	⁹⁸ Zhenzhen Guo et al.
Black linen cloth and expanded polyethylene	~93	400-1000	-	⁹⁹ Guilong Peng et al.
Combination structures				
Hierarchical surface nanostructure on copper surface	98	200-800	-	¹⁰⁰ Peixun Fan et al.
NiO (M-NiO) disc (TiAlON-based nanocomposite absorber)	98	350-1000	0.23	¹⁰¹ Huidong Liu et al.
CuCr ₂ O ₄ /SiO ₂ composite membrane	75, 44	300-800, 1500-2500	0.05	¹⁰² Yusuf Shi et al.
Cotton strand coated with a photothermal layer of polydopamine as a wick	97.5, 93.8	300-800, 800-1400	0.04	¹⁰³ Xuan Wu et al.
Electro- spun hydrophobic polyvinylidene fluoride (PVDF) nanofibers and hydrophilic carbon black/polyacrylonitrile (CB/PAN) composite	98.6	250-2500	0.08	¹⁰⁴ Tingting Gao et al.
Attapulgite/ poly acrylamide composite	99	250-2500	0.07	¹⁰⁵ Juan Jia et al.
Bilayered hybrid biofoam composed of bacterial nanocellulose (BNC)	96	400-1100	0.46	¹⁰⁶ Qisheng Jiang et al.
Cermet coated on a copper sheet, polystyrene foam disk, bubble wrap	-	-	0.03	²² George Ni et al.
Mxene Ti ₃ C ₂	~92	200-800	-	¹⁰⁷ Renyuan Li et al.
Bacterial nanocellulose (BNC) densely loaded with polydopamine (PDA)	94	450-750	0.44	¹⁰⁸ Qisheng Jiang et al.
Ag/diatomite combined with a filter paper	-	-	0.04	¹⁰⁹ Jing Fang et al.
Mesoporous Fe ₃ Si aerogel	-	-	0.04	¹¹⁰ Fengyu Zhang et al, J. Mat Chem A
Copper sulfide (CuS) films	85	400-2500	0.67	¹¹¹ Zhenzhen Guo et al.

obtained in this study with a solar thermal efficiency of 82% and evaporation rate of 1.3 kgm⁻²h⁻¹. Carbon black is a cost effective carbon based material which has garnered significant interest. Carbon black is used as a nanoparticle suspension in a few studies^{42,43}. Tingting Gao et al⁴⁴ developed a flexible material paradigm based on carbon black for high efficiency solar steam generation under 1 sun. Polyvinylidene fluoride nanofibers which has extremely low thermal conductivity is used as the bottom layer and carbon black/polyacrylonitrile composite is used as the top absorbing layer. This carbon black based flexible, cost effective structure has a solar thermal efficiency of 82% under 1 sun while having a evaporation rate of 1.2 kgm⁻²h⁻¹. In an interesting study by Jianjian Wang et al.¹¹², porous carbon was synthesized from cokes obtained as a side product of the zeolite catalyzed reactions. This carbon obtained was used by depositing it on a cellulose membrane for solar steam generation. It was seen that the carbon obtained had interconnected pores and tunable compositions. This unique carbon based structure showed an efficiency of 72% under 2 suns for solar steam generation. In a unique application of this concept by Sajadi et al.²⁷, a carbon based material paradigm was used to generate high pressure steam. The material consisted of a porous polymer skeleton coated with exfoliated graphite. The artificially-networked 3D veins provided path for liquid flow and exfoliated graphite has ~97% absorption in the solar spectrum. The structure produces steam at temperatures between 100-156 °C and pressure of 100-525 kPa. This work opened a wide range of applications where high pressure steam is required for power generation.

3.2.2 Plasmonic materials

Another class of materials that are being used for solar steam generation are plasmonic particles. Nanoscale plasmonic particles exhibit strong light absorption and also good light to heat conversion abilities. This is governed by a phenomenon called plasmonic resonance. It is triggered when the natural frequency of the electrons on the particles coincide with the photo frequency of the incident light. This results in the generation of hot electrons which subsequently results in the generation of heat^{24,113}. Several metallic nanoparticles including Gold (Au), Silver (Ag), Aluminium (Al), Germanium (Ge), Copper, Molybdenum, Cobalt, Nickel and Platinum are used for solar evaporation. A work by Haichuan Jin et al.¹¹⁴ investigated steam generation mechanism of gold nanoparticles based volumetric solar receivers. They showed that initial phase of steam generation is not due to nanobubble formation around the heated particles as predicted in earlier studies. It is due to localized solar absorption in the area where boiling and subsequent evaporation occurs. Increasing concentration of dispersions led to higher efficiencies while maintaining the bulk fluid at subcooled states. They obtained a photothermal conversion efficiency of 80.3% for a solar concentration of 220 suns and 12.75 ppm Au nanoparticles dispersion. In order to develop a scalable approach for the utilization of plasmonics, Yanming Liu et al.⁷⁰ developed a material paradigm using airlaid paper with extremely low thermal conductivity as the substrate for Au nanoparticles. This material paradigm is portable and can be recycled 30 times. Using this technology, they achieved localized plasmonic heating while maintaining the bulk liquid at ambient temperature. The evaporation efficiency was increased to 77.8% in comparison with free standing plasmonic film which is

about 47.8%. One of the main concerns with the use of plasmonic nanoparticles for solar steam generation is their inability to absorb the entire range of the solar spectrum. In a recent work by Lin Zhou et al.¹¹⁵, they developed a plasmonic material based on Au nanoparticles and nanoporous templates. This plasmonic material absorbs ~99% throughout the visible and mid infrared regions between 400 nm and 10 μm. Therefore, they were able to obtain an efficiency of ~90% under 4 sun. In a similar work, also by Lin Zhou et al.¹¹⁶, using Au nanoparticles and alumina (Al₂O₃) template, a plasmonic material paradigm was developed to absorb ~90% of the wavelengths in the solar spectrum between 550 nm and 2500 nm while achieving an evaporation efficiency of ~50%.

3.2.3 Wood based materials

Wood based materials have been extensively studied for solar steam generation. Natural wood has open and aligned microchannels and are used by trees for transpiration. Inspired by this, Guobin Xue et al.⁸² used flame treated natural wood as their solar absorber since it has high absorbance in the solar spectrum and the open and aligned microchannel in natural wood help in the fluid transport to the liquid-vapor interface. They reported an evaporation efficiency of 72% under one sun. Mingwei zhu et al.¹¹⁷ showed 99% absorption in the solar spectrum and efficient solar steam generation with long term stability in seawater without salt accumulation using carbonized mesoporous wood. However, in this approach, since the material is not flexible, it cannot be scaled up easily. In order to address this issue, Chaoji chen et al.⁸¹ developed a flexible wood surface modified with CNTs. This structure has ~98% absorption in the solar spectrum due to the CNTs, hierarchical micro and nanochannels for fluid flow to the interface, flexibility due to the nature of the material matrix and an efficiency of ~81% at 10 sun solar irradiation.

3.2.4 Plant based materials

Recently, in an attempt to move towards naturally abundant materials, various plant based materials are being explored for solar heat localization. Among these materials, carbonized mushroom was used effectively for solar steam generation by Ning Xu et al.⁸⁹. Efficient solar steam generation by mushrooms is attributed to its unique properties including umbrella shaped black pieus, porous nature and fibrous stipe with small cross section. Due to these properties, they have excellent absorption in the solar spectrum, good water transport and vapor escape while having low thermal conductivity. In this work, foam is used to support the mushroom at the liquid vapor interface. Excellent evaporation efficiency of ~78% was obtained using carbonized mushrooms at 1 sun solar concentration. Following this study, several mushroom based structures have been used for solar evaporation including artificial mushrooms from polyvinyl alcohol sponge coated with charcoal⁹⁵. Shendong Zhuang et al.¹¹⁸ used carbonized leaf as an interfacial solar absorber. They coated the leaf with carbon black and evaluated its evaporation performance under low solar concentration of 0.3 sun. An evaporation rate of ~0.17 kgm⁻²h⁻¹ was observed. Yaixin zhang et al.⁵² used the porous nature of carbonized moldy bread for solar steam generation. Low thermal conductivity of 0.4 Wm⁻¹K⁻¹ and high

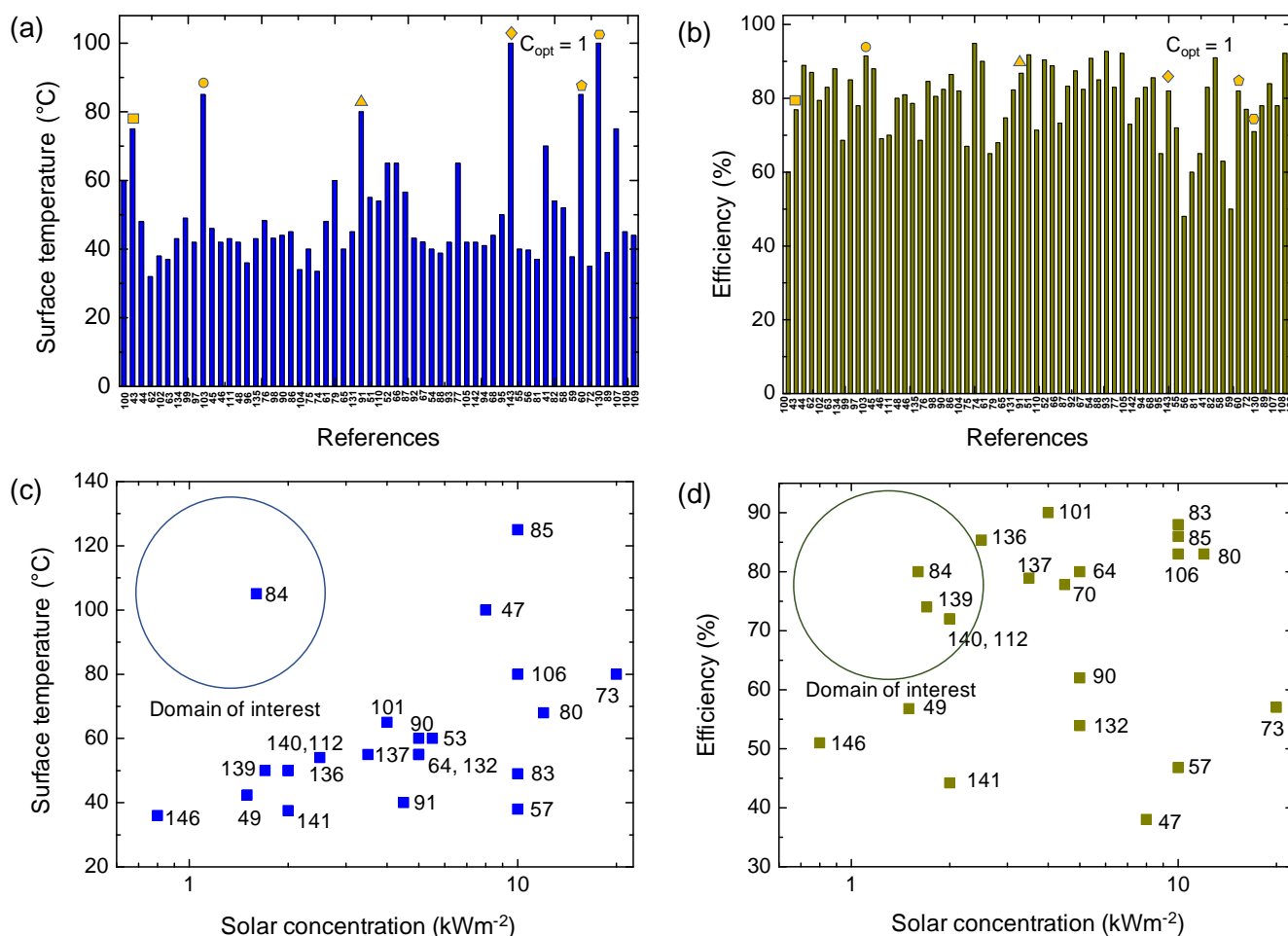


Figure 5 Figures of merit for power generation. (a) Surface temperature is shown for various works at solar irradiation of 1 kWm⁻². Outliers having high surface temperature are indicated. A surface temperature of ~ 100 °C has been achieved at ambient solar concentration. (b) Thermal efficiency for evaporation is shown for various works at solar irradiation of 1 kWm⁻². The outliers in (a) are also indicated here for comparison. (c) and (d) Surface temperature and efficiency are shown as functions of solar concentration. Domain of interested is indicated in both cases. High surface temperatures and efficiency are desired at low solar concentrations for cost effective technologies.

surface temperature of 65 °C is reported at 1 sun solar concentration.

3.2.5 Polymer based materials

Several polymeric materials are also used as solar absorbers including polypyrrole (PPy), polyvinyl alcohol (PVA)/PPy hybrid hierarchically nanostructured gels, polydopamine, and poly(1,3,5-hexahydro-1,3,5-triazines). These polymer based materials are also popularly used for desalination¹¹⁹. Lianbin Zhang et al.¹²⁰ used PPy as the photothermal polymer because of its broad spectrum absorption and low thermal conductivity. The PPy-coated meshes exhibit excellent porosity and the surface modification using fluoroalkylsilane reduces its surface energy. The surface exhibits high adhesion to water droplets and has enhanced water penetration. The material produces an evaporation rate of 0.92 kg m⁻²h⁻¹ and an evaporation efficiency of ~ 58% under 1 sun solar irradiation. Polyaniline (PAN) is another popularly used and studied polymer. It is recognized for its high light absorption in the visible and NIR regions of the solar spectrum¹²¹. Weichao Xu et al. used Janus membrane which is a

combination of a hydrophobic CB/PMMA light absorbing top layer coupled with a hydrophilic PAN bottom layer. Since each of these layers are independently designed; desired properties can be incorporated for high efficiencies.

3.2.6 Semiconductor-based materials

Semiconductor materials made from low cost, abundantly available elements having wide range absorption in the solar spectrum have emerged as a new class of photothermal materials. Several types of these materials have been studied such as metal oxide based¹²² and narrow bandgap semiconductors such as Ti₂O₃ nanoparticles¹²³ and black titania¹²⁴, bimetal oxides such as ZnFe₂O₄ and even trimetal oxides^{125,126}, MoO₃ quantum dots¹²⁷, and hierarchical copper phosphate¹²⁸. Copper sulphides are another class of compounds that have garnered attention recently. Cu₁₂Sb₄S₁₃ nanoparticles show full spectrum solar absorption and photothermal heating effect¹²⁹. Several studies have concentrated on lowering the bandgap to absorb solar energy in the full spectrum range. Wang et al. reduced

the intrinsic large bandgap of titanium dioxide of ~ 3 eV to ~ 0.1 eV. They claim a $\sim 92\%$ external solar-thermal efficiency¹²³.

4. Applications of heat localization and solar driven interface evaporation

4.1 Power generation

Effective technologies for solar power generation center around solar steam generation. This steam can be used to run the power producing unit (e.g. Turbines). In conventional technologies for solar steam generation, a material/surface absorbs the incident solar irradiation, and transfers this heat to a bulk fluid with the help of an intermediate carrier liquid. Furthermore, the generated steam is in thermal equilibrium with the bulk liquid and these systems work under high optical concentrations, thereby undergoing tremendous optical and surface losses^{11,13}. The concept of heat localization and interfacial evaporation was introduced to mitigate these losses by creating the hot spot at the liquid-vapor interface using buoyant solar absorber. Key components required to develop an efficient solar driven interfacial evaporation system are:

- solar absorber:** which has high absorption in the solar spectrum. It needs to absorb and convert the incident solar radiation into heat. The solar absorber also determines the surface temperature of the material structure.
- Floating evaporation structure:** An important aspect of a device for interfacial evaporation is that it must float at the liquid vapor interface while supplying the underlying water to the heated region, thereby ensuring high evaporation rate.
- Thermal insulator:** In order to facilitate heat localization at the liquid-vapor interface and provide maximum efficiency for evaporation, it is important to make sure that there is minimal heat loss to the underlying bulk liquid. This is done by providing thermal insulation in the evaporator.

The figures of merit for solar steam generation are as follows: solar concentration, surface/vapor temperature, thermal efficiency and evaporation rate. These parameters are listed for various studies employing the concept of solar driven interfacial evaporation for solar steam generation in **Table 2**. **Figure 5** shows the comparison between figures of merits in different studies. In the case of solar steam generation for power generation, it is desired to have high surface temperature and high thermal efficiency for evaporation at low solar concentrations. **Figs. 5a** and **5b** show surface temperature and efficiency under 1 kWm^{-2} solar irradiation for material paradigms used in various works. The average surface temperature in these studies is ~ 40 °C. However, few outliers exist where temperatures as high as 100 °C have been achieved at 1 sun. In order to have a comparative understanding of surface temperature and efficiencies, the surface temperatures of these studies in **Fig. 5a** are indicated with their corresponding efficiencies in **Fig. 5b**. Studies with high surface temperatures and efficiencies are discussed in further sections. **Figs. 5c** and **5d** show the surface temperatures and efficiencies under higher optical concentrations. The desired domain of interest which is high surface temperature, high efficiency and low solar concentration is marked in these figures. Although there are few studies in this domain of interest, their drawbacks in terms of scalability and long term implementation are elaborated in future

sections. Initially, in order to tackle the drawbacks of the conventional bulk boiling process, Neumann et al.²⁰ used Au nanoparticles as volumetric absorbers as shown in **Fig. 6a**. On illumination, these light-absorbing nanoparticles reached temperatures much above the boiling point of water. The vapor formed at the particle-liquid interface and on continued illumination, the vapor volume increased and reached the liquid-vapor interface. The vapor eventually was released, the nanoparticles returned to solution and this process repeated continuously. This was one of the first reported studies where interfacial evaporation was explored as opposed to conventional bulk boiling. However, the solar concentration used for generation of steam in this work was in the order of 10^3 kWm^{-2} . This high optical concentration requires complex cost intensive systems which are not desired. In order to mitigate this drawback, Ghasemi et al.²¹ proposed the concept of heat localization and a carbon based material paradigm for steam generation at low solar concentration and high efficiency. Using this concept, an efficiency of 85% was obtained 10 kWm^{-2} . In this study, exfoliated graphite was used as the solar absorber and carbon foam as the insulating layer as shown in **Fig. 6b**. The bottom carbon foam layer had small pore size for underlying liquid to reach the heated top surface and the top exfoliated graphite layer had larger pore size for vapor to escape. Therefore, the absorber localizes the solar energy and reaches a high temperature creating a hot spot, the fluid wicks to the hot spot internally where the evaporation occurs. The underlying liquid stays at ambient temperature, thereby preventing heat losses and increasing solar thermal efficiency significantly. Following this work, several other works explored materials and technologies to achieve solar steam generation low solar concentrations and high efficiencies by tuning the above-mentioned parameters. Several materials have been studied for this application including carbon-based materials, plasmonic materials, wood based materials, polymeric and carbonized plant based materials to name a few. These categories of materials have been explained in detail in an earlier section. In this section, we elaborate various unique works on solar interfacial evaporation for power generation and their figures of merits.

In an interesting work by Sajadi et al.²⁷, the concept of heat localization was used to produce high pressure (100-525 kPa) and high temperature (156 °C) steam as shown in **Fig. 6c**. This material paradigm being flexible, offered a path for large-scale implementation. The flexible material is composed of a porous polymer matrix containing exfoliated graphite as the solar absorber. The porous matrix has interconnected 3D veins for fluid flow to the interface through wicking. The material structure has extremely low thermal conductivity of $0.26 \text{ Wm}^{-1}\text{K}^{-1}$ and the exfoliated graphite used as the solar absorber has an absorption of $\sim 97\%$ in the solar spectrum. This technology and relevant material paradigm extended the reach of heat localization to high pressure applications.

George Ni et al.¹³⁰ developed a cost effective structure for solar steam generation under low concentration of 1 sun using the concepts of thermal concentration and heat localization as shown in **Fig. 6d**. While doing so, they achieved a vapor temperature of 100 °C under ambient conditions with an efficiency of 64%. Conventionally, for a blackbody absorber at 100 °C, ambient temperature of 20 °C and heat transfer coefficient, $h = 10 \text{ Wm}^{-2}\text{K}$, the convective heat loss is in the order of 800 Wm^{-2} and the radiative heat loss of 680 Wm^{-2} .

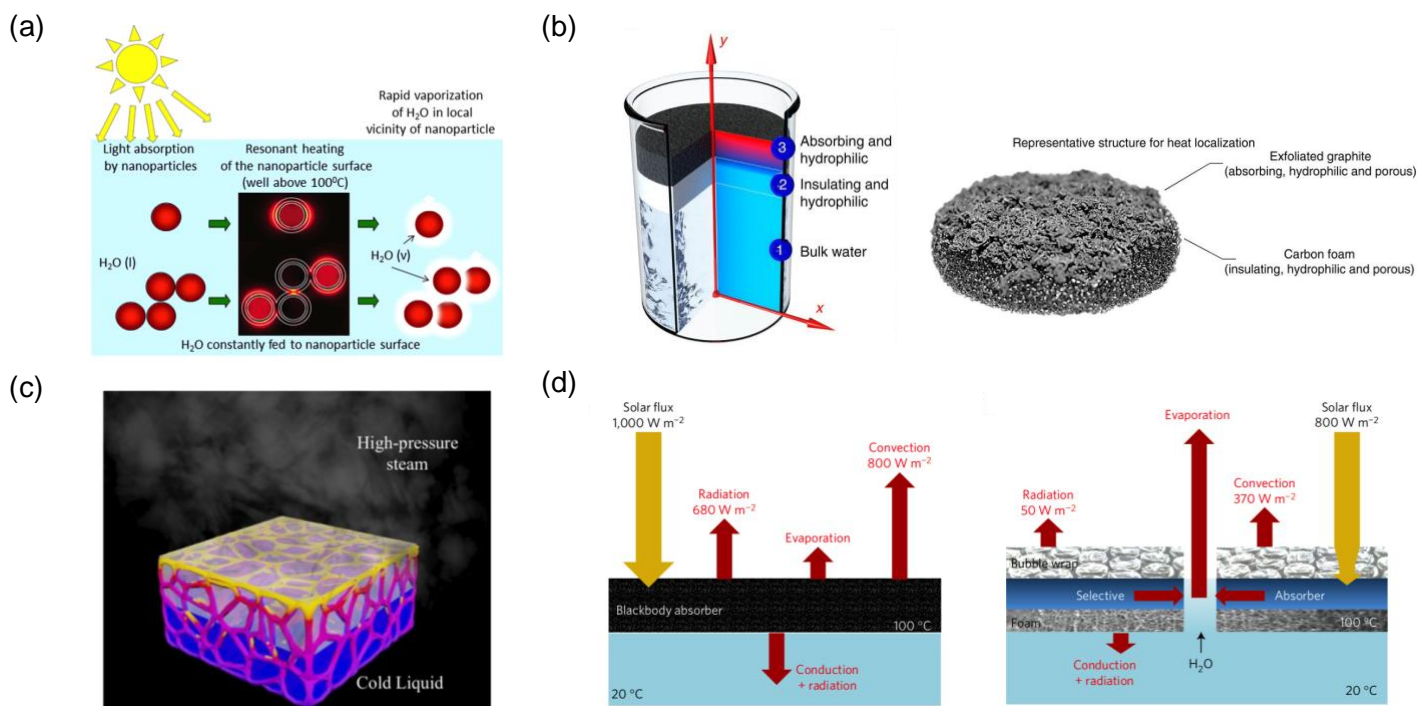


Figure 6 Concept of heat localization for power generation. (a) Plasmonic nanoparticles are used as alternate materials to achieve heat localization. They are tuned to achieve high absorption in the solar spectrum while achieving high surface temperatures. (b) The irradiated solar energy is localized at the liquid-vapor interface while preventing thermal losses and enabling high evaporation efficiency. A double layer structure is used with a exfoliated graphite top layer and porous carbon foam as the thermally insulating bottom layer. (c) The concept of solar heat localization was used to generate high pressure steam (100-525 kPa) while generating steam at temperatures between 100 and 156 °C. (d) Surface temperature of ~ 100 °C was achieved at ambient solar irradiation (1000 Wm⁻²) by a combination of heat localization and thermal concentration approaches. The material structure was optimized to reduce the surface losses when compared to a conventional black body absorber. Ref: Neumann et al²⁰, Ghasemi et al²¹, Sajadi et al²⁷ & Ni et al²².

This exceeds the incoming heat flux of 1000 Wm⁻². Therefore, in order to achieve boiling temperature of water at extremely low solar fluxes, it is required to minimize these heat losses. In this work, techniques are described to do so while using cost effective material paradigms. First, the blackbody absorber is replaced by a spectrally selective absorber (cermet coated on a copper sheet), which has high solar absorptance α and low thermal emittance ϵ . This is done so that sunlight is absorbed, and minimal back radiation occurs. Secondly, thermal insulation is used both on the top and bottom surfaces of the selective absorber (polystyrene foam disk). Next, the concept of thermal concentration is used where the absorbed heat is conducted into the evaporation area which is much smaller than the absorber's surface area. By doing so, the convective losses were reduced to 370 Wm⁻² and radiative losses to 50 Wm⁻² for an incoming solar flux of 800 Wm⁻². In addition, a large transparent bubble wrap was used as the top surface to minimize the convective losses. In order for the underlying liquid to reach the selective absorber, a dark fabric is placed in the center which holds a fabric wick. This wick goes through the foam to the underlying water. The water is drawn by the wick continuously and supplied to the selective absorber for evaporation. This was the first study to report a high vapor temperature of 100 °C for ambient solar concentrations (>1 sun). In an approach to develop flexible and durable material structures, Wu et al. developed a composite material containing CuS yolk-shell nanocages as the

photothermal material, cotton layer as the soft matrix and insulator and agarose hydrogel as the binding material between the CuS nanocages and the cotton. By doing so, they were able to obtain a highly flexible, durable material suitable for large scale implementation. They achieved a high water evaporation rate of 1.63 kgm⁻²h⁻¹ and ~93% in the UV-vis-NIR regions of the solar spectrum (290-1400 nm). In addition, cotton rods used in the composite material has extremely low thermal conductivity of ~0.04 Wm⁻¹K⁻¹. In order to achieve high efficiency solar steam generation, it is important to develop a scalable synthesis procedure where the pore dimensions can be controlled accurately. Yue Shao et al.¹³¹ developed hierarchically porous carbon membranes (HCMs) for this purpose. In the synthesis of these HCMs, pore sizes and porous architecture can be controlled by the selective use of anions in poly ionic liquids (PILs). The developed material is robust and has an efficiency of 74.69% under 1 sun. Among all the categories of materials used, plasmonics have either needed high optical concentrations for efficient solar energy harvesting or have suffered from low solar absorption when compared to other state-of-the-art materials. Lin Zhou et al.²⁵ fascinatingly developed a plasmonic material paradigm for solar steam generation which has a measured absorbance of ~99% in the solar spectrum (400nm to 1000nm). They used two components in achieve this absorption, the Au nanoparticles for the plasmonic effect and the wave guiding effect of

Table 2: Figures of merit for power generation

Type of material	Solar conc (kWm ⁻²)	Surface/ vapor temp (°C)	Evap rate (kgm ⁻² h ⁻¹)	Eff (%)	Reference
Hierarchical surface nanostructure on copper surface	1	60	-	60	¹⁰⁰ Peixun Fan et al
NiO (M-NiO) disc (TiAlON-based nanocomposite absorber)	4	65	5.25	90	¹⁰¹ Huidong Liu et al,
Ag@TiO ₂ core-shell nanoparticles	5	55	4.3	53.9	¹³² Haoran Li et al,
Black PAN/CB membrane on green leaf	0.3	43	0.21	37 (transpiration)	⁴² Shendong Zhuang et al
Modified graphene aerogel	1	75	1.2	76.9	⁴³ Yang Fu et al
Carbon coated paper on polystyrene foam	1	N/A (cold vapor generation)	2.2	88.9	¹³³ Haomin Song et al
Wood-polydopamine	1	75 (3.5 sun)	1	87	⁷⁸ Xuan Wu et al
Activated carbon fiber felt	1	48	1.22	79.4	⁴⁴ Haoran Li et al
Microporous zeolite structures	2	50	1.9	72	¹¹² Jianjian Wang et al
Nanoporous gold nanoparticle (AuNP)/poly(p-phenylene benzobisoxazole) nanofibre (PBONF) composite films	1	32	1.42	83	⁶² Meiling Chen et al
CuCr ₂ O ₄ /SiO ₂ composite membrane	1	38	1.32	88	¹⁰² Yusuf Shi et al
Ag@TiO ₂ nanoparticles	1	37	0.9	68.6	⁶³ Haoran Li et al
3D plasmonic solar absorber gel	1	43	3.8 (wind speed 6.3 ms ⁻¹)	85	¹³⁴ Minmin Gao et al
Au@TiO ₂ core-shell nanoparticles	5	55	3.96	80	⁶⁴ Jian Huang et al
Black linen cloth and expanded polyethylene	1	49	1.1	78	⁹⁹ Guilong Peng et al

Double-network hydrogel with a porous structure (p-PEGDA-PANi)	1	42	1.4	91.5	⁹⁷ Xiangyu Yin et al
Cotton strand coated with a photothermal layer of polydopamine as a wick	1	85	1.2	88	¹⁰³ Xuan Wu et al
Black titania/graphene oxide nanocomposite film affixed to airlaid paper, polyethylene foam	1	46	1.2	69.1	⁴⁵ Xinghang Liu et al
Carbon particles on the air-laid paper (C-paper)	1	42	0.96	70	⁴⁶ Shang Liu et al
Graphite nonwoven film	8	100	5	38	⁴⁷ Xiuqiang Li et al
Copper sulfide (CuS) films	1	43	1.1	80	¹¹¹ Zhenzhen Guo et al
Reduced graphene oxide and silk fabric	1	42	1.48	98	⁴⁸ Qian Zhang et al
Conjugated microporous polymer (CMP) aerogel	1	36	1	81	⁹⁶ Peng Mu et al
Tungsten oxide (WO _x) nanosheets	1	43	1.1	78.6	¹³⁵ Xin Ming et al
Graphite powder (GP) and a semipermeable collodion membrane (SCM)	1.5	42.4	1.36	56.8	⁴⁹ Fujun Tao et al
CuS nanoflowers and semipermeable collodion membrane (SCM)	1	48.3	1.09	68.6	⁷⁶ Fujun Tao et al
Coating a thin layer of carbon nanotubes (CNTs) on the top surface of a tree stump with roots	10	125	12	86	⁸⁵ Yilin Wang et al
Crumpled graphene balls	1	-	1.45	84.6	⁵⁰ Wei Hao et al
PEGylated MoS ₂ -cotton cloth	1	43.2	1.5	80.5	⁹⁸ Zhenzhen Guo et al
Polypyrrole (PPy) coated cotton fabric	1	44	1.2	82.4	⁹⁰ Dandan Hao et al
Carbonized Lotus seedpods	1	45	1.3	86.5	⁸⁶ Jing Fang et al
Electro-spun hydrophobic polyvinylidene fluoride (PVDF) nanofibers and hydrophilic carbon	1	34	1.2	82	¹⁰⁴ Tingting Gao et al

black/polyacrylonitrile (CB/PAN) composite					
Hydrophobic Fe ₃ O ₄ @C core-shell nanostructures	1	40	1.07	67	⁷⁵ Rong Chen et al
Cotton, photothermal CuS yolk-shell nanocages and agarose aerogel	1	33.5	1.63	94.9	⁷⁴ Xuan Wu et al
Nitrogen-doped graphene/carbon hybrid aerogel	1	48	1.6	90	⁶¹ Bingbing Huo et al
Hierarchical TiN nanotube mesh	2.5	54	2.7	85.36	¹³⁶ Peng Ren et al
Bi-layer system (C-wood)	1	60	1	65	⁷⁹ Xiao Luo et al
Graphene oxide	3.5	55	1.4 g/h	78.9	¹³⁷ Mustafa Ghafurian et al
C-Au-TiO ₂	1	40	0.97	68	⁶⁵ Jian Huang et al
Heteroatom-doped hierarchically Porous carbon membrane	1	45	1	74.69	¹³¹ Yue Shao et al
PPy-coated membranes	1	80	1.4	82.3	⁹¹ Canzhu Wang et al
Monolithic carbon-aerogel	1	55	1.5	86.8	⁵¹ Peng Mu et al
Mesoporous Fe ₃ Si aerogel	1	54	2.08	91.8	¹¹⁰ Fengyu Zhang et al
Au nanocages (AuNCs) into electrospun nanofibers of poly(vinylidene fluoride) (PVDF)	0.4 W/cm ²	130	2	60	¹³⁸ Tong Wu et al
Carbonized moldy bread	1	65	1.2	71.4	⁵² Yaixin Zhang et al
Plasmonic covellite CuS hierarchical nanostructure	1	65	1.5	90.4	⁶⁶ Fujun Tao et al
Reduced graphene oxide wrapped plant fiber sponges (PFS@rGO)	1	56.6	1.4	88.8	⁸⁷ Tingjie Chen et al
Surface modified polyurethane (PU) sponge	1	43.2	1.35	73.3	⁹² Zheng Zhang et al
Superhydrophobic carbon black (CB) nanoparticles	5.5	60	2.74	-	⁵³ Miaomiao Ye et al
Gold nanospheres and nanostars are assembled	1	42.1	1.3	83.3	⁶⁷ Guofen Song et al

into ridges/disordered nanohole arrays					
Carbon foam based porous media	1.7	50	2.2	74	¹³⁹ F. M. Canbazoglu et al
Patterned surfaces by printing carbon black on the air-laid paper	1	40	1	-	⁵⁴ Yini Luo et al
Surface-carbonized de-sugaring stems of sugarcane	1	38.8	1.5	87.4	⁸⁸ Jie Liu et al
Porphyrin-based molecules	2	50	3	72	¹⁴⁰ Liyong Chen et al
Flexible porphyrin organic framework	1.6	105	1.95	80	⁸⁴ Zi-Jing Xia et al
Kapok fibers-PPy aerogels	1	42	1.4	82.4	⁹³ Peng Mu et al
TiO ₂ nanotubes/Ti gauze	2	37.5	1.41	44.2	¹⁴¹ Chaorui Xue et al
Tungsten carbide (WC) nanoarray film	1	65	1.06	90.8	⁷⁷ Nana Han et al
Attapulgite/ poly acrylamide composite	1	42	1.2	85	¹⁰⁵ Juan Jia et al
Carbon dots within microchannels of processed wood	1	42	2.27	92.7	¹⁴² Qiao Hou et al
Polypyrrole (PPy) wood	1	41	1.33	83	⁹⁴ Wei Huang et al
Cu nanoparticles within the carbon decorated oxygen-vacancy-rich TiO ₂ matrix	1	44	1.5	92.2	⁶⁸ Xiangcheng Zhang et al
Artificial mushroom made of the common poly- vinyl alcohol sponge coated with charcoal,	1	50	1.1	73	⁹⁵ Xiujun Gao et al
Porous Graphene sheet	1	100	1.5	80	¹⁴³ Yoshikazu Ito et al
Graphene Aerogel	1	40	1.62	83	⁵⁵ Xiaozhen Hu et al
Bilayered hybrid biofoam composed of bacterial nanocellulose (BNC)	10	80	11.8	83	¹⁰⁶ Qisheng Jiang et al
3D Printed CNT-GO and CNT-NFC	1	39.7	1.25	85.6	⁵⁶ Yiju Li et al
Wood graphene oxide composite	12	68	18.9	83	⁸⁰ Keng-Ku Liu et al

F-Wood/CNTs membrane	1	37	1.1	65	⁸¹ Chaoji Chen et al
Carbon Nanotube Membrane on Macroporous Silica Substrate	1	70	1.25	82	⁴¹ Yuchao Wang et al
Flame treated wood	1	54	1.1	72	⁸² Guobin Xue et al
Functionalized graphene	1	80 (3.6 sun)	0.52	48	¹⁴⁴ Junlong Yang et al
Carbon nanotube nanofluid	10	38	8.5	46.8	⁵⁷ Xinzhi Wang et al
rGO/mixed cellulose esters	1	52	0.9	60	⁵⁸ Gang Wang et al
rGO polyurathene nanocomposite foam	1	37.7	1	65	⁵⁹ Gang Wang et al
rGO with polystyrene foam	1	85	1.31	83	⁶⁰ Le Shi et al, 2017
Copper mesh, graphadiyne, CuO nanowires	1	59 (5 sun)	1.55	91	⁶⁹ Xin Gao et al
Au nanoparticles with airlaid paper supporting layer	4.5	40	1.71	77.8	⁷⁰ Yanming Liu et al
Self-assembly of metallic nanoparticles onto a nanoporous template	1		0.8	63	¹¹⁵ Lin Zhou et al
Plasmonic nanoparticles (Au/NPT)	1		0.61	50	¹¹⁶ Lin Zhou et al
Nanolayers of Reusable Biomimetic Nanoparticles	1	35	2.8	82	⁷² Changxu Liu et al
Copper sulphide nanocrystals	1			77	¹⁴⁵ Changbo Zhang et al
Silicon nanoparticles	0.8	36	0.48	51	¹⁴⁶ Satoshi Ishii et al
Cermet coated on a copper sheet, polystyrene foam disk, bubble wrap	1	100	1.72	71	¹³⁰ George Ni et al
Flexible thin-film black gold membranes	20	80	12.6	57	⁷³ Kyuyoung Bae et al
Natural and carbonized mashroom, carb mash	1	39	0.2	78	⁸⁹ Ning Xu et al
Mxene Ti ₃ C ₂	1	75	1.04	84	¹⁰⁷ Renyuan Li et al
Different natural woods	10	49	12	88	⁸³ Chao Jia et al

Oxygen-deficient molybdenum oxide quantum dots (MoO ₃ x QDs)	5	60	4.95	62	⁹⁰ Dandan Ding et al
Bacterial nanocellulose (BNC) densely loaded with polydopamine (PDA)	1	45	1.13	78	¹⁰⁸ Qisheng Jiang et al
Ag/diatomite combined with a filter paper	1	44	1.39	92.2	¹⁰⁹ Jing Fang et al
Ti ₂ O ₃ nanoparticles	1	50	1.32	92.1	¹²³ Juan Wang et al

the aluminum oxide (AAO) nanoporous nanochannels. The AAO membrane, through internal reflections scattered the light within nanoporous structure (porosity >40%) and functioned as an effective trapping medium. On the other hand, the Au nanoparticles having random sizes and distributions enable a high density of hybridized localized surface plasmon resonance (LSPR) which plays a pivotal role in effective absorption of light in a wide range of wavelengths. Under 4 sun solar irradiation, this material structure exhibited an evaporation rate of $\sim 6 \text{ kg m}^{-2} \text{ h}^{-1}$ with an evaporation efficiency of $\sim 90\%$. Kyuyoung Bae et al.⁷³ proposed an alternate strategy to improve solar absorption by Au nanoparticles. In this work, they propose adiabatic nanofocusing of plasmons with small taper angles ($\sim 1^\circ$) for efficient solar energy generation. It is proposed that this enables high surface plasmon dissipation losses for heat generation and high absorption in the metal structure. Using incorporate this concept, self-aggregated metallic nanowire array was mounted on a microporous substrate to produce a flexible thin film black gold membrane. These materials have 91% absorption in the complete solar spectrum between 400 to 2500 nm. However, they have extremely low thermal efficiency of 57% at solar irradiation of 20

kW m^{-2} . Although the solar absorption by plasmonic materials has been increased multiple folds, this technology still remains extremely cost intensive and further studies are being carried out to obtain this wide range of absorption in the solar spectrum with low cost plasmonic materials. The thermal efficiencies for solar steam generation by these materials are still lower when compared to other state-of-the-art materials at low solar concentrations.

4.2 Desalination

Desalination is a prominent and widely studied application of heat localization and interfacial evaporation. With 1.6 billion or almost one quarter of the world's population facing economic water shortage, new efficient technologies are urgently needed to tackle this issue as shown in Fig. 7a^{147,148}. Solar desalination is being viewed as a viable solution for the global water crisis with accelerated research being undertaken in this domain of study. Various components of a structure for solar desalination are shown in Fig. 7b. In this application, the steam generated by solar heat localization is condensed to obtain pure water for various applications. The salts in the saline solution are precipitated/separated while keeping a

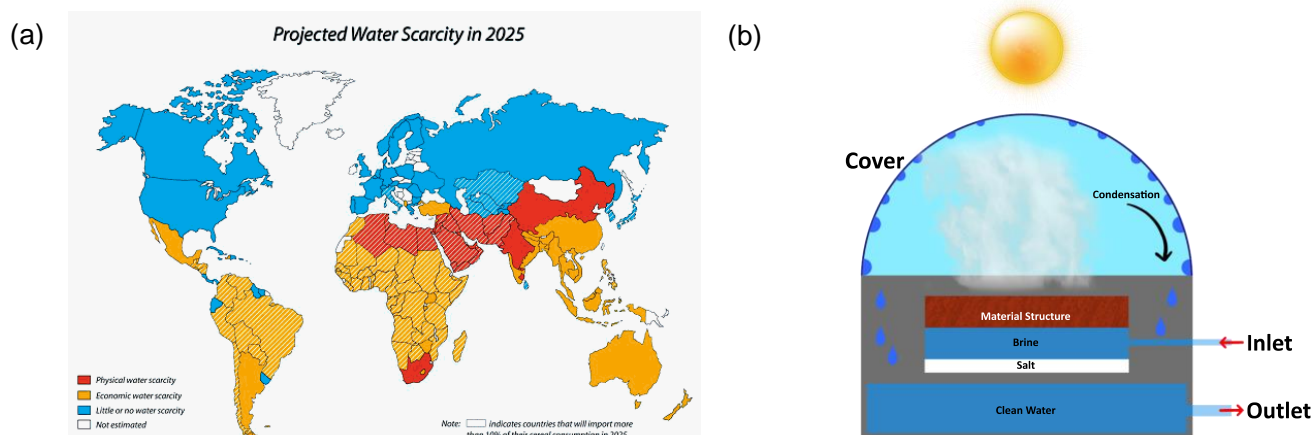


Figure 7 Concept of solar heat localization for desalination. (a) Water scarcity is an extensive problem all over the world. It is projected that almost >50% of the world will face water crisis within the next 10 years. (b) The main components needed for solar desalination are highlighted. A cover structure is utilized for desalination systems to act as a simultaneous condensation unit, to collect the pure water. Anti-fouling/ anti-clogging techniques help in continuous long-term operation of these systems.

Ref: fewresources.org.

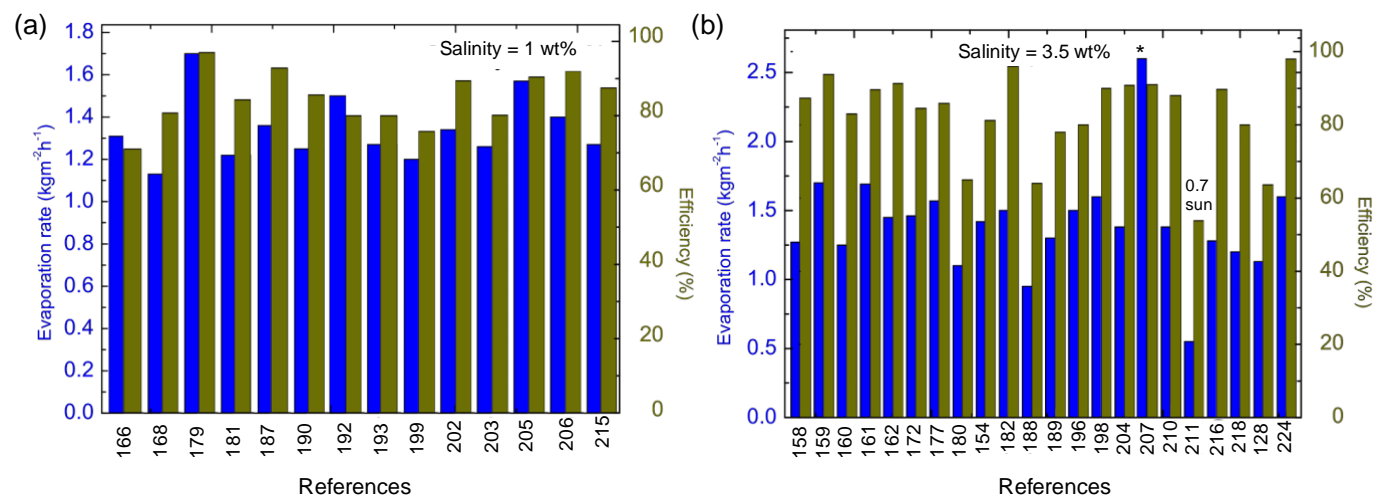


Figure 8 Figures of merit for desalination. Evaporation rates and efficiencies are shown for various studies for concentrations of salt in solution of 1 and 3.5 wt%, Note that the solar concentration in all the cases are 1 kWm^{-2} unless specifically mentioned. The enthalpy of liquid vapor phase change has been altered in a few studies and they have been indicated. Note that * denotes $h_{LV} = 1250 \text{ kJ/kg}$ due to nanoconfinement of water in the polymer matrix.

constant and high evaporation rate. The key figures of merit required for efficient solar desalination include high rate of evaporation for highly saline solution, high evaporation efficiency, durability, low solar concentration and most importantly anti-fouling/anti-clogging capabilities for long term operation. In addition, a flexible material paradigm is desired for long term implementation. In **Table 3**, these figures of merit are listed for various works on solar desalination using heat localization and interfacial evaporation. **Figure 8 and Figure 9** show the comparative study of evaporation rates and thermal efficiencies reported in various works as a function of salt concentrations used in solutions. This gives a wholistic understanding of the state-of-the-art studies conducted and provides us an insight on necessary improvements required for enhanced performance. Several structures have been developed recently towards solar desalination including graphene oxide based materials^{36,149}, carbon nanotube-silica bi layer⁴¹, modified PTFE membrane¹⁵⁰ and Anodized aluminum oxide (AAO) membrane¹⁵¹ to name a few. However, one key figure of merit that has not been addressed in most of the works is fouling of the material structure for long duration operation. In the subsequent section, several material structures and relevant technologies reported for solar desalination are discussed in detail.

In a recent interested study, Fei Zhao et al.¹⁵² developed a hierarchically nanostructured gel based on polyvinyl alcohol (PVA) and polypyrrole (PPy) for high efficiency solar desalination. Moreover, they showed that the evaporation of these gels remained unaltered for 28 days of operation for salinities upto 10 wt%. The performance of this material paradigm is attributed to the energy confinement strategy through the hierarchical water pathways in the hydrogels. These pathways consist of micron channels and molecular meshes. The water in these molecular meshes have reduced vaporization enthalpy which contribute to high evaporation rates and efficiency under ambient conditions. PPy is used as the solar absorber which penetrated into the polymeric gel PVA. The solar energy absorbed by the PPy is directly transferred to the water in the molecular meshes for evaporation. Furthermore, due to the usage of

micron channels for fluid transport, rapid water diffusion takes place, thereby continuously supplying the fluid for evaporation. Since PVA is used as the matrix to hold the fluid for evaporation, the PVA chains also reduce the convective heat loss from the fluid which is a major source of heat loss in state-of-the-art studies. By this approach, an extremely high evaporation rate of $3.2 \text{ kgm}^{-2}\text{h}^{-1}$ is obtained with a thermal efficiency of 94% under 1 sun solar irradiation. It shown that this evaporation rate can be obtained over several days for solar desalination while obtaining solar water purification yield of 20.3 Lm^{-2} . However, it is not mentioned clearly as to how the problem of fouling is addressed in this work. Lin Zhou et al.¹⁵³ used aluminum nanoparticles for solar desalination. Localized heating of these Al nanoparticles was enabled by plasmon hybridization and localized surface plasmon resonance. The final structure was prepared by self-assembly of these Al nanoparticles into a 3D porous membrane. This structure has an absorption of 96% in the solar spectrum (400 to 2500 nm). They report an evaporation rate of $5.7 \text{ kgm}^{-2}\text{h}^{-1}$ and a thermal efficiency of 88.4% at 4 sun solar irradiation. Solar desalination experiments were conducted for 25 cycles with a 10 wt% saline solution. Negligible drop in evaporation rate was observed. Furthermore, they characterized the plasmonic structure for salt residue before and after 25 cycles using SEM imaging. No change in penetration depth or salt crystals were observed in the pores. Furthermore, on washing the sample with DI water, salt residue was observed in the washed solution. However, they claim that the salt residues can be washed off completely even after long term desalination. In another interesting approach to prevent salt crystallization on the surface of the material, Yun Xia et al.¹⁵⁴ spatially isolated the crystallization sites for salts from the water evaporation surface as shown in **Fig. 10a**. By doing so, they were able to achieve continuous solar desalination and salt recovery for over 600 hours. The material structure consists of horizontal evaporation disc and a

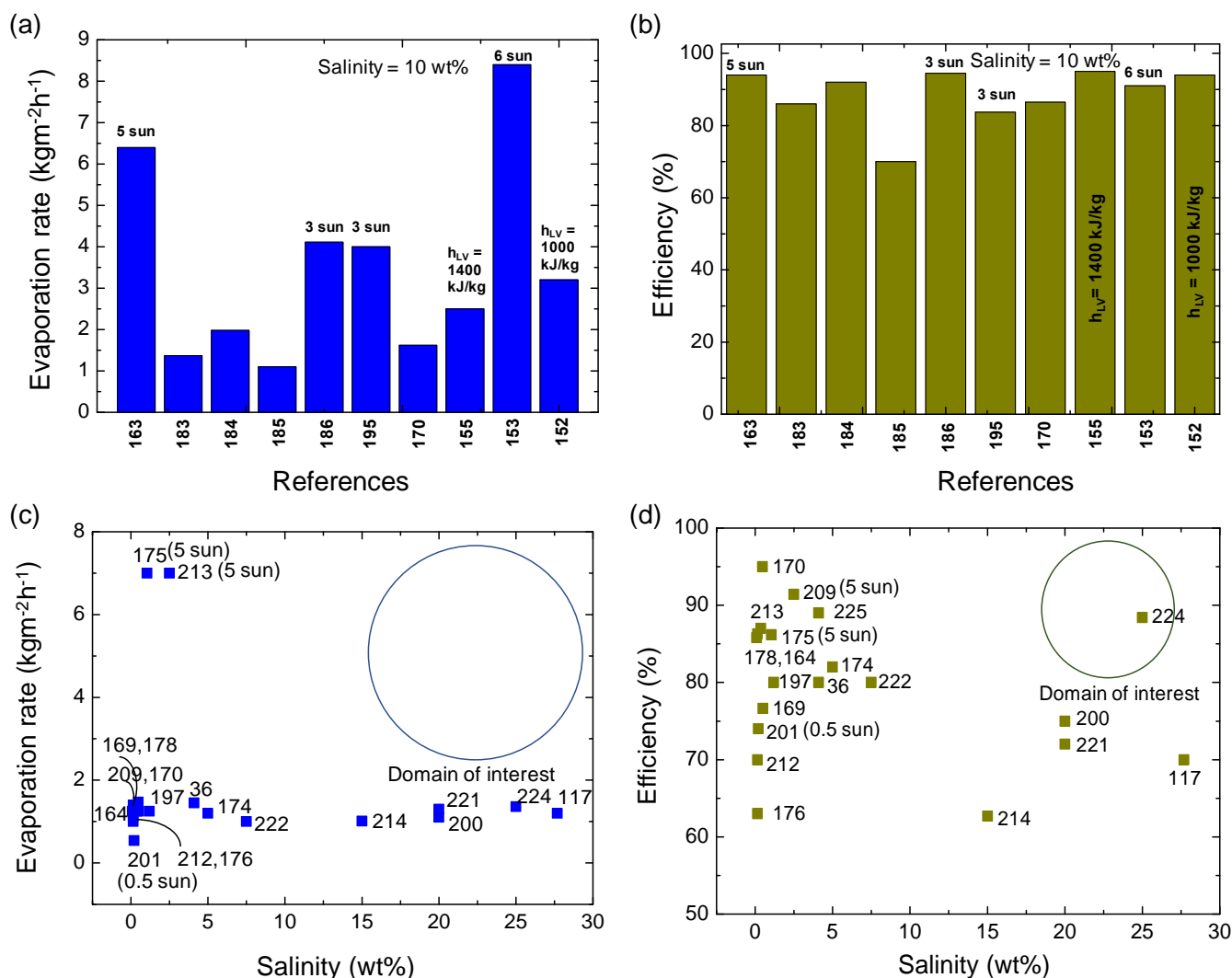


Figure 9 Figures of merit for desalination. (a) and (b) Evaporation rate and efficiency is shown for various studies for a concentration of salt in solution of 10 wt%. The enthalpy of liquid-vapor phase change has been altered in a few studies which have been indicated above. (c) and (d) Evaporation rate and efficiency is shown as a function of all other salt concentrations. The domain of interest which is high salinity of solution and high evaporation rate and efficiency are indicated. Although the average salt concentration in the sea is ~ 3.5 wt%, several studies have accounted for saturated salt solutions and the salinity of dead sea (10 wt%). Note that the solar concentration in all the cases are 1 kWm^{-2} unless specifically mentioned.

vertical solution uptake thread. The evaporation disc consists of three layers including a light absorbing layer (CNTs), a water spreading layer (filter paper) and a thermal insulating layer (polystyrene foam). The wicking to the absorption surface takes place by a cotton thread. The salt solution is transported to the disc and the radial concentration gradient is regulated from the center to the edge of the disc. This process takes place due to the spreading of the liquid by the super-hydrophilic filter paper which is integrated in the evaporation disc. Simultaneously during this transport process, the water evaporates due to the localized heat on the solar absorber (CNTs). Subsequently, the salt concentration in the remaining solution increases and reaches the edge of the disc eventually to crystallize. Therefore, the salt only accumulated at the edges and not on the central evaporation surface. Eventually, as the binding force decreases between the salt crystal and the disc, it drops under gravity.

In a study by Kashyap et al.²⁶, a mechanism was reported to develop an anti-clogging material paradigm for long term solar desalination as shown in **Fig. 10b**. The flexible, roll-able nature of this material structure is suitable for large scale implementation. Here, exfoliated graphite and carbonized rayon are used as solar absorbers. These solar absorbers are embedded into a liquid latex matrix to make a composite material structure. The anticlogging properties of this material was achieved by the combination of specially designed pore dimensions based on the agglomerate size of salt particles and use of PEDOT-PSS as an antifouling coating. PEDOT-PSS facilitates poor adhesion of salt to the surface of the material and since the agglomerate size of the salt particles is lower than the pore dimension, the salt particles fall back into the brine solution due to gravitational force and are deposited at the bottom of the container. Continuous desalination was reported using this material for upto 20 hours with no drop in evaporation rate ($1.01 \text{ kgm}^{-2}\text{h}^{-1}$) and thermal

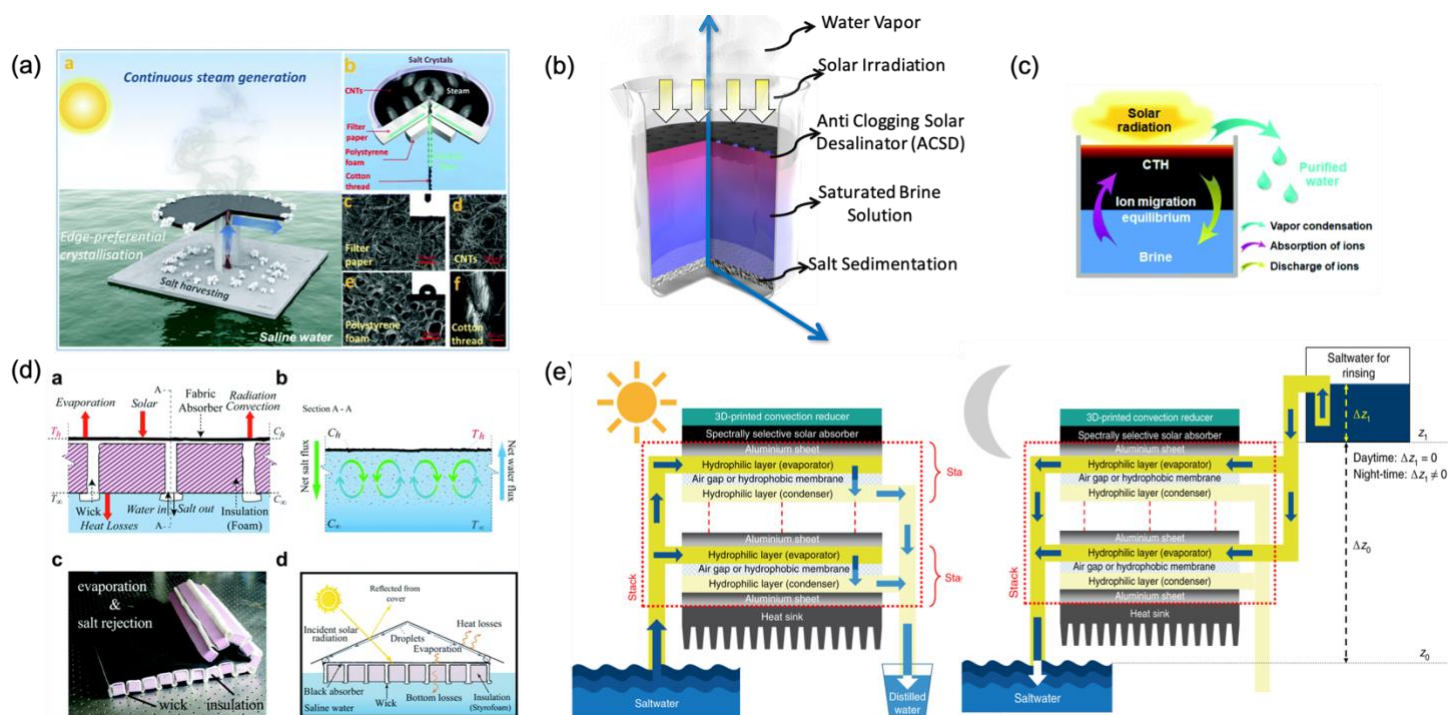


Figure 10 Methods to prevent salt accumulation. Several works have proposed ways in which salt accumulation can be prevented for continuous solar desalination systems. (a) Edge preferential crystallization and subsequent removal due to gravity was used to achieve continuous solar desalination for ~ 600 hours without any salt accumulation on the evaporation surface. (b) A combination of custom designed pore sizes based on agglomerate size of salt particles and a PEDOT-PSS anti-fouling coating on the surface of the absorber was used to prevent salt accumulation, thereby providing long term solar desalination for > 20 hours of operation. (c) Using the concepts of diffusion and advection for salt rejection, a cost effective solar still was fabricated for prolonged desalination on the surface of the ocean. (d) A modular multi-layer design was employed for desalination of water both during day and night cycles. The salt concentration gradient is utilized in this case to wash off the accumulated salt during night operation. Ref: Xia et al¹⁵⁴, Kashyap et al²⁶, Zhou et al¹⁵⁵, Ni et al²⁵² and Chiavazzo et al¹⁵⁷.

efficiency (62.7%) at 1 sun solar concentration. Furthermore, experiments were conducted for solar concentrations of 0.75 sun and also under outdoor conditions to obtain similar anti-clogging properties.

Another material structure for long term solar desalination of > 100 h was reported by Xingyi Zhou et al.¹⁵⁵ having antifouling properties to prevent salt accumulation. The material contains a hybrid hydrogel composed of a hydrophilic PVA polymer and reduced graphene oxide (rGO) solar absorber. The rGO solar absorber has excellent absorption in the solar spectrum and the material structure has internal capillary channels that facilitate continuous fluid transport for evaporation. Due to these properties, a high evaporation rate of $\sim 2.5 \text{ kg m}^{-2} \text{ h}^{-1}$ was obtained. This evaporation rate, which is approximately twice that of conventional systems at one sun is due to lowering of the enthalpy of liquid-vapor phase change. This is done by the principle of nanoconfinement wherein the -OH groups in the polymer matrix form hydrogen bonds with the water molecules leading to the formation of intermediate water and subsequent reduction in the enthalpy. The ion concentration of salt residuals in the material remained constant for 96 hours of continuous operation, thereby proving crystalline antifouling functionality of the material. This is due to the equilibrium between salt ion absorption and salt ion discharge due to diffusion as shown in Fig. 10c.

George Ni et al.¹⁵⁶ developed a floating solar still for scalable desalination as shown in Fig. 10d. Conventional solar stills which are used for desalination in low infrastructure environments for solar desalination. However, they operate with low efficiencies of ~ 20 -40% and are cost intensive. In this work, the concept of solar interfacial evaporation is incorporated in conventional solar stills to develop a low cost technology for solar desalination. The floating still incorporating the concept of heat localization, rejects the salt and prevents fouling on its surface. By doing so, it can operate for prolonged durations while producing desalinated water at a rate of $2.5 \text{ L m}^{-2} \text{ day}^{-1}$. The material structure consists of a top solar absorbing layer (black cellulose fabric). This fabric also wicks up the water. An insulating layer consisting of alternating layers of polystyrene foam and white cellulose fabric is placed underneath the black fabric which insulated the top layer from the underlying fluid and also helps in rejecting the salt back to the fluid. The white cellulose cloth also wicks the underlying fluid to the black fabric. Salt rejection happens either by diffusion or by advection down the fabric wick. Considering diffusion as the major contributor, the salt concentration difference between the salt accumulation on the evaporation surface and the bottom liquid drives the salt rejection process.

A modular structure was proposed by Chiavazzo et al.¹⁵⁷ for low cost solar desalination as shown in Fig. 10e. The modular structure

Table 3: Figures of merit for desalination

Type of material	Solar con (kWm ⁻²)	Surface/vapor temp(°C)	Evap rate (kgm ⁻² h ⁻¹)	Eff (%)	Salinity (wt%)	Reference
Carbonized melamine foams	1	42	1.27	87.3	3.4	¹⁵⁸ Xiaofeng Lin et al
3D photothermal cone (polypyrrole (PPy) coating layer)	1	46	1.7	93.8	3.5	¹⁵⁹ Yuchao Wang et al
Polymeric nanofibers as the matrix and inorganic carbon black nanoparticles	1	42	1.25	83	3.5	¹⁶⁰ Yong Jin et al
Vertically aligned graphene sheets membrane	1	42.5	1.69	89.6	3.5	¹⁶¹ Linfan Cui et al
Black carbonized wood, ailaid paper, polyethalene foam	1	50.4	1.45	91.3	3.5	¹⁶² Peng-Fei Liu et al
Bilayer Janus, film by assembling gold nanorod (AuNR) onto the interconnected single-walled carbon nanotube	5	55	6.4	94	10	¹⁶³ Yanbing Yang et al
Ink-stained paper-black	1	44	1.25	85.8	0.1	¹⁶⁴ Ziyang Deng et al
Graphene membrane	1	-	1.37	90	-	¹⁶⁵ Guijun Li et al
Ti ₃ C ₂ nanosheet layer on a hydrophobic MXene membrane	1	-	1.31	71	1	¹⁶⁶ Jianqiu Zhao et al
Porous CuS/polyethylene (PE) hybrid membrane		30.6	1.3	63.9	-	¹⁶⁷ Mengya Shang et al
Nonstoichiometric W ₁₈ O ₄₉ mesocrystal	1	41	1.13	80.7	1	¹⁶⁸ Yuhong Chang et al
Multiwalled carbon nanotubes (MWCNTs) nanofluids	1	57.1	1.25	76.65	0.5	¹⁶⁹ Wenjing Chen et al
Vertically ordered pillar array of graphene-assembled framework	1	38.5	1.47	95	0.48	¹⁷⁰ Panpan Zhang et al

3D solar evaporator from a silica/carbon/silica (SCS) trilayered coaxial fibrous membrane	1	47	1.36	88.4	25	¹⁷¹ Yusuf Shi et al
Monocrystallized Cu ₂ ZnSnS ₄ (CZTS) nanosheet-assembled membrane	1	44.5	1.46	84.5	3.5	¹⁷² Chunhong Mu et al
Hydrophobic PVDF-HFP nanofibers electro-spun directly on the surface of PVA sponge surface	1	48	0.98	72	0.6 M	¹⁷³ Guobin Xue et al
Cu nanodot-embedded N-doped graphene urchins	1	70	1.2	82	5	¹⁷⁴ Jijian Xu et al
CuFeSe ₂ nanoparticles (NPs) decorated wood	5	51.5	7	86.2	1.05	¹⁷⁵ Hanwen Liu et al
PGPU nanocomposites containing Au and Ag nanoparticles	1	80 (5 sun)	1	63	0.15	¹⁷⁶ Fathi S. Awad et al
Carbonized daikon	1	49	1.57	85.9	3.5	¹⁷⁷ Mengmeng Zhu et al
Plasmonic Functionalized Cotton with Au and Ag nanoparticles	1	90 (8 sun)	1.4	86.3	0.15	¹⁷⁸ Kiriarachchi et al
Molybdenum nitride nanorambutans	1	51	1.7	97	1	¹⁷⁹ Lin Zhu et al
SiC-C composite monoliths	1	68.3	1.1	65	3.5	¹⁸⁰ Le Shi et al
Metal-organic framework (MOF) derived porous carbon	1	36.9	1.22	84.3	1	¹⁸¹ Sainan Ma et al
Carbon nanotubes (CNTs)	1	50	1.42	81.2	3.5	¹⁵⁴ Yun Xia et al
Metal-organic-framework-based hierarchical structure	1	55	1.5	96	3.5	¹⁸² Qinglang Ma et al
Silicon-copper membrane consisting of hierarchical nanoscale hybrids	1	59.6	1.37	86	10	¹⁸³ Xiaoying Song et al

Melamine sponges (MS)	1	43.3	1.98	92	10	¹⁸⁴ Feng (Frank) Gong et al
Carbon nanotubes (CNTs) and fire-resistant inorganic paper based on ultralong hydroxyapatite nanowires (HNs)	1	38	1.1	70	10	¹⁸⁵ Zhi-Chao Xiong et al
g-C ₃ N ₄ /graphene hybrid hydrogel	3	41	4.11	94.5	10	¹⁸⁶ Hui Su et al
Ag nanoparticles modified floating carbon cloth	1	37	1.36	92.82	1	¹⁸⁷ Panzhe Qiao et al
Microporous graphite foam coated with carbon nanoparticle	1	50	0.95	64	3.5	¹⁸⁸ Gyoung Gug Jang et al
Bamboo charcoal	1	50	1.3	78	3.5	¹⁸⁹ Zhengtong Lee et al
Oxygen-defected molybdenum oxides hierarchical nanostructure	1	60	1.25	85.6	1	¹⁹⁰ Qichen Lu et al
Reduced graphene oxide (RGO)/cotton fabric on vertically oriented porous polyacrylonitrile foam (VOPPF)	1	~40	1.5	-	3.5	¹⁹¹ Panzhe Qian Zhang et al
Artificial tree of carbon nanotubes (CNTs) film/paper hybrid	1	70	1.5	80	1	¹⁹² Peng Xiao et al
MoS ₂ and expandable polyethylene	1	40	1.27	80	1	¹⁹³ Rong Chen et al
Hollow carbon spheres	1	-	1.6	-	3.5	¹⁹⁴ A. Celzard et al
CNT dyed cotton	3	45	4	83.7	10	¹⁹⁵ Hui Kou et al
CNT functionalized Eggshell membrane	1	40.5	1.5	80	3.5	¹⁹⁶ Xiao Han et al
Candle soot coated cotton	1	44	1.25	80	1.2	¹⁹⁷ Higgins M et al
Black gold nanoparticles-deposited sponge	1	90	1.6	90	3.5	¹⁹⁸ Yizhen Liu et al
Wasted rice straw	1	37.1	1.2	75.8	1	¹⁹⁹ Qile Fang et al

Artificial channel-array in a natural wood substrate	1	-	1.1	75	20	²⁰⁰ Yudi Kuang et al
Graphene aerogel beads	0.5	34.3	0.54	74	0.2	²⁰¹ Xiaming Feng et al
Bilayer aerogel, hydroxyapatite (HAP) nanowire and carbon nanotube (CNT)	1	44	1.34	89.4	1	²⁰² Dong-Dong Qin et al
Three-dimensional carbon foams	1	60	1.26	80.1	1	²⁰³ Pengxiang Qiu et al
Polystyrene sulfonate (PSS)@Cu ₃ (BTC)3•3H ₂ O (HKUST-1)/single-walled carbon nanotube (SWCNT) (PHS) membrane	1	50	1.38	90.8	3.5	²⁰⁴ Xu Ma et al
Melamine foam	1	43	1.57	90.4	1	²⁰⁵ Chenwei Li et al
Multilayer PPy nanosheets	1	45	1.4	92	1	²⁰⁶ Xu Wang et al
Polyvinyl alcohol and activated carbon	1	38.1	2.6	91	3.5	²⁰⁷ Youhong Guo et al
Foldable GO film	1	38.8	1.45	80	4.1	³⁶ Xiuqiang Li et al
Vertically Aligned Graphene Sheets Membrane	1	39.7	1.62	86.5	10	²⁰⁸ Panpan Zhang et al
Hierarchical graphene foam	5	60	7	91.4	2.5	²⁰⁹ Huaying Ren et al
Carbon black and hydrophilic porous paper	1	44.2	1.38	88	3.5	²¹⁰ Zhejun Liu et al
NP- mediated photothermal heating in a membrane desalination geometry	0.7	35	0.55	53.8	3.5	²¹¹ Pratiksha Dongare et al
Carbonized wood	10		1.2	70	27.69	¹¹⁷ Mingwei Zhu et al
rGO with magnetic nanoparticles (MNP)	1	47	1.12	70	0.15	²¹² Xiangqing Wang et al
3D cross-linked honeycomb graphene foam material	1	40	1.25	87	0.37	²¹³ Yang Yang et al

Carbonized rayon, liquid latex	1	43	1.01	62.7	15	²¹⁴ Kashyap et al
Porous carbon black/graphene oxide composite layer, polystyrene matrix	1	38	1.27	87.5	1	²¹⁵ Yiju Li et al
Paper-based reduced graphene oxide (PrGO) composite membrane on top of a silicone-based porous insulation layer	1	80	1.28	89.7	3.5	²¹⁶ Zizhao Wang et al
Vertically aligned CNTs	15	43	22	90	1	²¹⁷ Zhe Yin et al
Black cellulose fabric, polystyrene	1	42		57	3.5	¹⁵⁶ George Ni et al
Carbon based polymer foam	1	46	1.2	80	3.5	²¹⁸ Qiaomei Chen et al
Polyvinyl alcohol, PVA and reduced graphene oxide, rGO	1	32	2.5	95	10	¹⁵⁵ Xingyi Zhou et al
Al Nanoparticles	6	100	8.4	91	10	¹⁵³ Lin Zhou et al
Plasmonic membranes (Au NPs)	10	97	11.5	85	1	²¹⁹ Xinzhi Wang et al
Plasmonic wood (metallic NPs)	1	55	1	68		²²⁰ Mingwei Zhu et al
Hierarchically nanostructured gel (HNG) based on PVA and polypyrrole (PPy)	1	45	3.2	94	10	¹⁵² Fei Zhao et al
Janus absorber (CB, PMMA and PAN)	1	60 (6 sun)	1.3	72	20	²²¹ Weichao Xu et al
Nanotube MoS ₂ hybrid film	1	50 (5 sun)	1	80	7.5	²²² Xiangdong Yang et al
Hierarchical microstructured copper phosphate	1	44	1.13	63.6	3.5	¹²⁸ Zhentao Hua et al
Al-Ti-O nanostructure	0.82		0.5	77.52		²²³ Luocai Yi et al
Pigment/quartz glass fibrous composite	1	42	1.6	98	3.5	²²⁴ Yusuf Shi et al
Plasmonic-active filter paper (PP)	10	85 (10 sun)	11.97	89	4.1	²²⁵ Zhipeng Liu et al

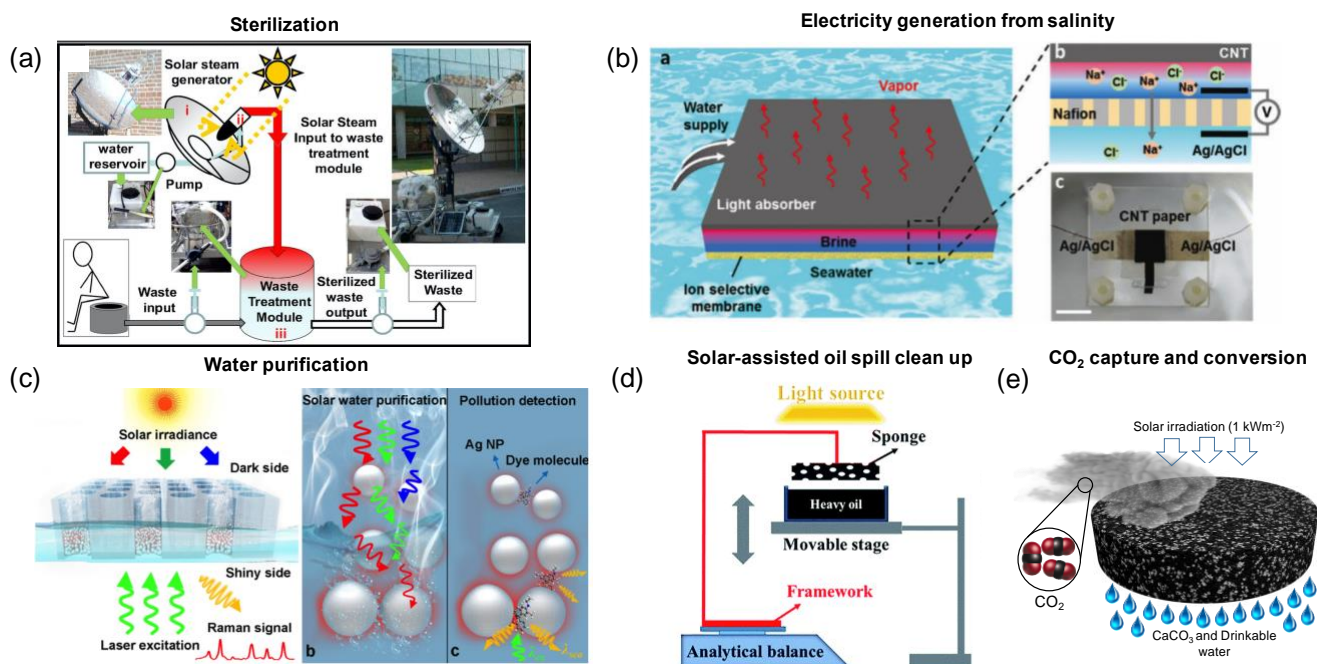


Figure 11 Other applications of solar heat localization. Various works on different applications of solar heat localization are highlighted here. (a) A compact sterilization system was designed using plasmonic nano particles to produce steam at ~ 132 °C for 5 minutes with solar concentration. (b) An ion selective membrane (nafion) is used to harvest electricity from the salt concentration difference between the bulk sea water and the water underneath the absorber. (c) Plasmonic nanoparticles (Ag) are used to achieve water purification using solar heat localization. Controlled amount of contaminants are added to the initial solution and the resulting liquid after purification is verified. (d) A CNT modified polyurethane sponge is used for oil clean up from the surface of water using solar heat localization. On reaching elevated temperatures, the sponge heats the heavy oil, thereby reducing its viscosity and facilitating its absorption by the sponge. (e) Graphene aerogel impregnated with ionic liquids is used for enhanced CO_2 capture. This reusable structure is used to convert the captured CO_2 to calcium carbonated. Ref: Neumann et al²²⁸, Yang et al²²⁹, Chen et al²³¹, Chang et al²⁴⁸ & Kashyap et al²³².

consists of two hydrophilic layers separated by a hydrophobic microporous membrane. Here, the latent of condensation of the distillate is recovered by multiple evaporation/condensation stages. Another interesting aspect of this modular device is its ability to exploit low-temperature heat without the need for mechanical components. By using this concept, the multi stage device was able to obtain desalinated water at $2.95 \text{ Lm}^{-2}\text{h}^{-1}$ under 900 Wm^{-2} solar flux. A key aspect of this work is the mechanism for salt removal. The physics of diffusion is used for this purpose. The salt accumulation mainly occurs in the hydrophilic layers used as evaporators. The high salinity water in the evaporator diffuses back into the saltwater source during the nights. In addition to this, salt removal is also aided by gravity due to density variations between high and low salinity solutions.

Several other strategies have been explored for salt rejection including hydrophobic membrane^{221,226,227}, microchannels²²⁰ and washing^{160,209}. In a work by Yang et al²²⁶, anti-fouling copper-zinc-tin-selenide assembled membrane is used for solar desalination and to prevent salt accumulation for prolonged periods of time (up to 30 days). Here, salt concentration gradient is promoted by using a hydrophobic and the salt dissolves into the bulk liquid by diffusion. In a similar strategy, Zhao et al²²⁷ used a hydrophobic Ti_3C_2 based metal carbide membranes to achieve a similar effect. Zhu et al

demonstrate that the open microstructures in plasmonic wood exhibit salt self-cleaning property. During the day, the salt concentrates on the top surface and during nights, the formed salt diffuse back into the bulk saline solution. Large diameter microchannels prevent blocking during 8-hour day cycles. Ren et al²⁰⁹ use graphene foam for enhanced solar desalination. In this study, under 1 sun solar irradiation, due to large diameter of pores on the foam ($>50 \mu\text{m}$), no channel blockage is observed for 7.5 hours. However, for higher solar concentration, salt can be removed from the material by washing/rinsing in the bulk fluid for reusing.

4.3 Other applications

Along with power generation and desalination, solar heat localization and interfacial evaporation has found applications in several other domains including water purification, distillation, sterilization, water splitting, solar driven oil clean-up, electricity generation from salinity and CO_2 capture. In this section, we elaborate on each of the above-mentioned applications while studying the role of interfacial evaporation and solar heat localization in each application. **Table 4** lists the figures of merit required for efficient performance in these applications. Dongare et al²¹¹ used nanoparticles driven photothermal heating to develop a concept for solar membrane distillation. The nanoparticles are

embedded within the surface layer of the membrane. The feed water passes through one side of the membrane and due to localized heating, reaches elevated temperatures and subsequently vaporizes. This vapor condenses on the distillate side of the membrane. Therefore, this localized heating using nanoparticles eliminates the need to heat the saline solution externally, increasing the efficiency of the system. At the highest temperature, the evaporation rate was $\sim 0.55 \text{ kg m}^{-2} \text{ h}^{-1}$ and an efficiency of 53.8% was obtained at 0.7 kW m^{-2} . This system was also tested for desalination using 3.5 wt% salt concentration solution. However, long term durability have not been addressed in this study.

High temperature ($>100 \text{ }^\circ\text{C}$) steam for prolonged is desired for distillation/sterilization applications. Another system was developed by Neumann et al.²²⁸ using broadband light harvesting nanoparticles for solar distillation. In this study, as shown in **Fig. 11a**, a compact solar autoclave is designed for off-grid applications. Using solar concentrators (Fresnel lens or dish mirror), steam at a temperature of $\sim 135 \text{ }^\circ\text{C}$ can be delivered and this temperature can be maintained by the developed system for 5 minutes. Furthermore, this steam is delivered to a 14.2 L capacity commercially available sterilization volume. The capacity of a mobile sanitation toilet being only 10L, it can be easily accommodated in this system.

In another interesting application of solar heat localization, Yang et al.²²⁹ demonstrated simultaneous steam and electricity generation in their system as shown in **Fig. 11b**. As shown in the figure, the structure consists of multiple layers. The top light absorbing layer localizes the heat to achieve high surface temperatures. The seawater is supplied to the surface through capillary force (wicking mechanism) for continuous evaporation. In addition to this, an ion selective membrane (Nafion) is used along with Ag/AgCl as the electrode system. A concentration gradient is developed due to rapid evaporation between the bulk liquid and the water beneath the material structure. This concentration gradient on the two sides of the ion selective membrane, provides the ability to generate electricity. This system has an evaporation rate of $1.1 \text{ kg m}^{-2} \text{ h}^{-1}$ while having a thermal efficiency of 75%. In addition to this, an output power of $\sim 1 \text{ W m}^{-2}$ is measured at 1 sun solar concentration. Water purification is a widely studied application of interfacial evaporation with a critical footprint in human daily lives.

Solar thermoelectric generators are also recently explored to generate electricity directly in various works^{47,230}. In an innovative application, Li et al.⁴⁷ integrated solar interfacial evaporation and thermoelectric module to both obtain pure water and produce electricity. They used a graphite based flexible material as their solar absorber and generated steam at an evaporation efficiency of 81.7%. Subsequently, they condensed this steam to generate pure water. Using the temperature gradient between the steam on one side and ambient temperature on the other, the thermoelectric module produced an open circuit voltage of 3.87V. This voltage can be further increased by increasing the temperature of steam. Degradation of contaminants is a critical figure of merit for water purification using solar heat localization. Chen et al.²³¹ used silver (Ag) plasmonic structures for water purification using solar heat localization. The Ag nanoparticles are placed within a nanoporous template and the structure is asymmetric with a metallic surface on one side and a dielectric surface on the other as shown in **Fig. 11c**.

On illuminating from the top surface (dark side), the light is effectively absorbed by the nanoparticles along the longer path length. In addition to water purification, the closed packed Ag nanoparticles are also sensitive to detection of water pollutants.

One of the recent applications of heat localization has been in solar assisted cleanup of oil spills. In this interesting approach, carbon nanotube modified polyurethane sponge is used to selectively absorb oil when exposed to solar irradiation as shown in **Fig. 11d**. When exposed to solar irradiation, the CNT treated PU sponge localizes the heat and heats up rapidly. Subsequently, this material increases the temperature of the heavy oil on top of water. This heating reduces the viscosity of the oil by two orders to magnitude and the sponge absorbs oil equal to 20 times its own weight. The authors showed that 85% of the oil on surface of water was recovered in their experiments.

In the process of transitioning to renewable energy sources, carbon negative systems such as CO_2 capture mechanisms play a critical role. Currently, amine-based systems are used commercially for this purpose. However, due to formation of carbamate salts, it is extremely energy intensive to reuse these materials. Kashyap et al.²³² developed a sustainable CO_2 collector (SCC) which is activated by solar heat localization as shown in **Fig. 11e**. Ionic liquids which are known for high CO_2 absorption are integrated into a graphene aerogel matrix. Both static and dynamic flow experiments are conducted to determine CO_2 capture. For every mole of the ionic liquid, 0.2 moles of CO_2 is captured by this material. A simple washing process involving extremely low concentrations of $\text{Ca}(\text{OH})_2$ is used to convert the absorbed CO_2 into useful byproducts, including water and calcium carbonate. This precipitated calcium carbonate has multiple applications including the manufacture of paints, plastics, papers, and sealants. The reusability of this material for multiple cycles of operation is also demonstrated. With more materials being studied and innovated for improved efficiencies of these systems, many applications are emerging in this domain of study.

5. Conclusion

In this review, we provided a thorough definition of solar heat localization concept which has a promising future in a wide range of technologies. This concept efficiently harvests solar irradiation and converts it to thermal energy which is the driving force for a vast majority of industries including power generation, desalination, distillation and sterilization. The two main role players in implementation of this concept are the material type and its geometry implementation mechanism. The required material properties for solar heat localization are high absorption in the solar spectrum, low thermal conductivity, fast hydrodynamic of flow and buoyancy. These characteristics are implemented with a range of materials including carbon-based materials, polymers, natural materials, plasmonic materials and wood-based materials. All these advancements in material creation and synthesis are discussed. As long as the above material properties are satisfied, there is no performance advantage between individual material types. That is, solar heat localization is a general concept and can be implemented with various material paradigms. However, the type of desired

application may impose additional restrictions on the material. For example, for high temperature steam generation, durable materials

Table 4: Figures of merit for other applications

Water purification						
Type of material	Solar conc (kWm ⁻²)	Surface/Vapor temp (°C)	Evap rate (kgm ⁻² h ⁻¹)	Conc of pollutants (%)	Eff (%)	Reference
Silver nanoparticles	1	N/A	1	-	60	²³¹ Chuanlu Chen et al
Fe ₃ O ₄ nanoparticles decorated with TiO ₂ nanoparticles	1	40	2.75 g/h	85% degradation in pollutants	76.4	²³³ Lei Shi et al
Titanium Nanorods on Carbon Fabric	1	35.4	0.9	87% degradation in pollutants	87.5	²³⁴ M.W. Higgins et al
Cellulose ester (MCE) membrane, hedgehog-like hierarchical ZnO particles (HP) and gold nanoparticles (Au NPs)	1	50	0.1	70% degradation in pollutants	-	²³⁵ Xinzhi Wang et al
Graphene oxide and a multiscale plasmonic nanostructure	10	-	12.96	90% degradation in pollutants	92	²³⁶ Minmin Wang et al
Molybdenum disulfide (MoS ₂)	0.76	70	0.8	80% degradation of pollutants	80	²³⁷ Deoukchen Ghim et al
Carbon nanotubes (CNTs) based floating solar still	1	44.6	0.88	57% degradation of pollutants	-	²³⁸ Qimao Gan et al
Poly(N-isopropylacrylamide) hydrogel	1	55	4.2	~100% reduction in pollutants	-	²³⁹ Hongya Geng et al
TiO ₂ nanoparticles, Au NPs, AAO membrane	1	58	0.5	~60% reduction in pollutants	-	¹⁵¹ Yang Liu et al
rGO/ TiO ₂ composite	1	68.3	1.25 g/h	~94% reduction in pollutants	-	²⁴⁰ Jinwei Lou et al
Distillation						
Type of material	Solar conc (kWm ⁻²)	Surface/vapor temp(°C)	Evap rate (kgm ⁻² h ⁻¹)	Conc promotion (%)	Eff (%)	Reference
black polyurethane sponges	3	56.3	2.5	25 wt%	55	²⁴¹ Sainan Ma et al
Cu ₂ SnSe ₃ (or Cu ₂ ZnSnSe ₄) nanosphere arrays	1	43	1.66	10 wt%	86.6	²⁴² Yawei Yang et al

PPy-coated Stainless Steel mesh	1	-	0.92	-	58	¹²⁰ Lianbin Zhang et al
------------------------------------	---	---	------	---	----	------------------------------------

Sterilization					
Type of material	Solar conc (kWm ⁻²)	Surface/ vapor temp (°C)	Evap rate (kgm ⁻² h ⁻¹)	Eff (%)	Reference
rGO/PTFE composite membrane	2.2 W/cm ²	121	-	84	²⁴³ Yao Zhang et al
Biochar	1	132	1.21	80	²⁴⁴ Jinlei Li et al
Solar vacuum tube, air-laid paper and copper mesh	0.6	121	0.7	49	²⁴⁵ Chao Chang et al

Water splitting					
Type of material	Solar conc (kWm ⁻²)	Surface/ vapor temp (°C)	Evap rate (kgm ⁻² h ⁻¹)	Eff (%)	Reference
In-situ coating of nanoparticles on a commercial thermoelectric generator	1	44	0.9	58.6	²⁴⁶ Xiaofei Zhang et al
NEC/WSe ₂ /CF structure (carbon foam structure)	-	-	-	-	²⁴⁷ Zhaoyong Lin et al

Oil clean up						
Type of material	Solar conc (kWm ⁻²)	Surface/ vapor temp (°C)	Evap rate (kgm ⁻² h ⁻¹)	oil recovery Eff (%)	Oil viscosity (Pa.s)	Reference
Carbon nanotube (CNT) modified polyurethane sponge	1	78	-	90	110.87	²⁴⁸ Jian Chang et al
nanostructured TiO ₂ -coated copper	-	-	-	-	-	²⁴⁹ HaoRan Liu et al

Electricity generation from saline solution							
Type of material	Solar conc (kWm ⁻²)	Surface/vapor temp (°C)	Evap rate (kgm ⁻² h ⁻¹)	Eff (%)	Salinity (M)	Power (V)	Reference
Graphene/carbon cloth	1	45.4	1.5	83	0.5	0.37	²⁵⁰ Baofei Hou et al
CNT modified filter paper with Nafion membrane	1	-	1.1	73	-	-	²²⁹ Peihua Yang et al

at high temperatures (e.g. carbon-based) are needed. One overlooked aspect on development of materials for this concept is the dynamics of fluid flow in the structure. Also, for low solar concentration, it may not be an issue, but for high solar concentration's, the fluid transport should be taken into account to avoid any dry-out event in the materials which will degrade or defunctionalize the material. The transport mechanism in the material structure is governed by the surface characteristics and internal geometry of the material. Fluid interaction with the material becomes a critical issue in some of the applications such as desalination. As the fluid is a brine solution, any undesired dissociation of brine in the material structure leads to fouling in the structure and defunctionalizes the material structure in long-term. A range of innovative strategies are developed to address the fouling problem and provide long-term durable and efficient materials. Another important characteristic which is needed before large-scale implementation of this concept is mechanical, chemical and environmental durability of the material system in each specific application. Long-term exposure to UV may degrade polymers and this needs to be addressed in actual systems. Apart from the material type, geometry and implementation mechanism also play a critical role in performance of this concept. To minimize the losses to the surrounding environment, materials with 1D and 2D path flows are developed or the material structure is separated from the fluid reservoir.

Each application imposes its own figures of merit and these are tabulated in detail. These metrics along with cost and scalability of the material synthesis should be considered to adopt this concept for large scale implementation. Although power generation and desalination are the major applications for this concept, new emerging applications are offered recently such as water splitting and CO₂ capture. In general, any application that runs on thermal energy may adopt this concept (e.g. food processing).

We envision the growth of this field in three aspects simultaneously: (1) advancement of fundamental knowledge on the interaction of light and the material structure and the fluid interaction with the material, (2) synthesis and development of advanced materials for

solar heat localization for specific applications and (3) adoption of the current validated materials in small-scale or larger-scale either as a retrofit or as new systems. In the last six years, the multidisciplinary field of solar heat localization has gained immense interest from various communities including physics, chemistry, material science and engineering and various technological sectors and will continue in the upcoming years.

Conflicts of interest

Authors declare no conflicts of interest

Acknowledgements

The authors gratefully acknowledge funding support from the Air Force Office of Scientific Research for grant (AFOSR FA9550-16-1-0248) with Dr. Ali Sayir as program manager.

References

- 1 A. Meier, N. Gremaud and A. Steinfeld, *Energy Convers. Manag.*, 2005, **46**, 905–926.
- 2 G. W. Crabtree and N. S. Lewis, *Plant, Cell Environ.*, 2007, **30**, 37.
- 3 N. S. Lewis, *Science (80-.)*, 2016, **351**, aad1920–aad1920.
- 4 N. S. Lewis, *Science (80-.)*, 2007, **315**, 798–802.
- 5 M. Romero and A. Steinfeld, *Energy Environ. Sci.*, 2012, **5**, 9234.
- 6 A. Sari and A. Karaipekli, *Appl. Therm. Eng.*, 2007, **27**, 1271–1277.
- 7 H. Ghasemi, E. Sheu, A. Tizzanini, M. Paci and A. Mitsos, *Appl. Energy*, 2014, **131**, 158–170.
- 8 M. A. Shannon, P. W. Bohn, M. Elimelech, J. G. Georgiadis, B. J. Marinas and A. M. Mayes, *Nat. (London, U. K.)*, 2008, **452**, 301–310.
- 9 M. Ayub, A. Mitsos and H. Ghasemi, *Energy*, 2015, **87**, 326–

335.
10 M. Elimelech and W. A. W. Phillip, *Science (80-.)*, 2011, **333**, 712–717.
- 11 T. Fend, B. Hoffschmidt, R. Pitz-Paal, O. Reutter and P. Rietbrock, *Energy*, 2004, **29**, 823–833.
- 12 D. Jenkins, R. Winston, J. Bliss, J. O’Gallagher, A. Lewandowski and C. Bingham, *J. Sol. Energy Eng.*, 1996, **118**, 141.
- 13 A. Kribus, P. Doron, R. Rubin, J. Karni, R. Reuven, S. Duchan and E. Taragan, *Sol. Energy*, 2000, **67**, 3–11.
- 14 L. A. Weinstein, J. Loomis, B. Bhatia, D. M. Bierman, E. N. Wang and G. Chen, *Chem. Rev.*, 2015, **115**, 12797–12838.
- 15 H. Tyagi, P. Phelan and R. Prasher, *J. Sol. Energy Eng.*, 2009, **131**, 041004.
- 16 T. P. Otanicar, P. E. Phelan, R. S. Prasher, G. Rosengarten and R. A. Taylor, *J. Renew. Sustain. Energy*, , DOI:10.1063/1.3429737.
- 17 R. A. Taylor, P. E. Phelan, T. P. Otanicar, C. A. Walker, M. Nguyen, S. Trimble and R. Prasher, *J. Renew. Sustain. Energy*, , DOI:10.1063/1.3571565.
- 18 G. Ni, N. Miljkovic, H. Ghasemi, X. Huang, S. V. Boriskina, C. Te Lin, J. Wang, Y. Xu, M. M. Rahman, T. J. Zhang and G. Chen, *Nano Energy*, 2015, **17**, 290–301.
- 19 J. A. Eastman, S. U. S. Choi, S. Li, W. Yu and L. J. Thompson, *Appl. Phys. Lett.*, 2001, **78**, 718–720.
- 20 O. Neumann, A. S. Urban, J. Day, S. Lal, P. Nordlander and N. J. Halas, *ACS Nano*, 2013, **7**, 42–49.
- 21 H. Ghasemi, G. Ni, A. M. Marconnet, J. Loomis, S. Yerci, N. Miljkovic and G. Chen, *Nat. Commun.*, 2014, **5**, 4449.
- 22 G. Ni, G. Li, S. V. Boriskina, H. Li, W. Yang, T. Zhang and G. Chen, *Nat. Energy*, 2016, **1**, 16126.
- 23 T. A. Cooper, S. H. Zandavi, G. W. Ni, Y. Tsurimaki, Y. Huang, S. V. Boriskina and G. Chen, *Nat. Commun.*, 2018, **9**, 1–10.
- 24 P. Tao, G. Ni, C. Song, W. Shang, J. Wu, J. Zhu, G. Chen and T. Deng, *Nat. Energy*, 2018, **3**, 1031–1041.
- 25 L. Zhou, Y. Tan, D. Ji, B. Zhu, P. Zhang, J. Xu, Q. Gan, Z. Yu and J. Zhu, *Sci. Adv.*, 2016, **2**, e1501227.
- 26 V. Kashyap, A. Al-Bayati, S. M. Sajadi, P. Irajizad, S. H. Wang and H. Ghasemi, *J. Mater. Chem. A*, , DOI:10.1039/C7TA03977H.
- 27 S. M. Sajadi, N. Farokhnia, P. Irajizad, M. Hasnain and H. Ghasemi, *J. Mater. Chem. A*, 2016, **4**, 4700–4705.
- 28 C. Ishino, M. Reyssat, E. Reyssat, K. Okumura and D. Quéré, *Epl*, 2007, **79**, 8–12.
- 29 S. J. Kim, J. W. Choi, M. W. Moon, K. R. Lee, Y. S. Chang, D. Y. Lee and H. Y. Kim, *Phys. Fluids*, , DOI:10.1063/1.4914384.
- 30 J. Bico, C. Tordeux and D. Quéré, *Europhys. Lett.*, 2001, **55**, 214.
- 31 L. Courbin, E. Denieul, E. Dressaire, M. Roper, A. Ajdari and H. A. Stone, *Nat. Mater.*, 2007, **6**, 661–664.
- 32 N. Srivastava, C. Din, A. Judson, N. C. MacDonald and C. D. Meinhart, *Lab Chip*, 2010, **10**, 1148–1152.
- 33 J. Kim, M. W. Moon, K. R. Lee, L. Mahadevan and H. Y. Kim, *Phys. Rev. Lett.*, , DOI:10.1103/PhysRevLett.107.264501.
- 34 J. Kim, M.-W. Moon and H.-Y. Kim, *J. Fluid Mech.*, 2016, **800**, 57–71.
- 35 X. Li, R. Lin, G. Ni, N. Xu, X. Hu, B. Zhu, G. Lv, J. Li, S. Zhu and J. Zhu, *Natl. Sci. Rev.*, 2018, **5**, 70–77.
- 36 X. Li, W. Xu, M. Tang, L. Zhou, B. Zhu, S. Zhu and J. Zhu, *Proc. Natl. Acad. Sci. U. S. A.*, 2016, **113**, 13953–13958.
- 37 H. Liu, C. Chen, G. Chen, Y. Kuang, X. Zhao, J. Song, C. Jia, X. Xu, E. Hitz, H. Xie, S. Wang, F. Jiang, T. Li, Y. Li, A. Gong, R. Yang, S. Das and L. Hu, *Adv. Energy Mater.*, 2018, **8**, 1–8.
- 38 G. Liu, J. Xu and K. Wang, *Nano Energy*, 2017, **41**, 269–284.
- 39 Y. Ito, Y. Tanabe, J. Han, T. Fujita, K. Tanigaki and M. Chen, *Adv. Mater.*, 2015, **27**, 4302–4307.
- 40 X. Hu, W. Xu, L. Zhou, Y. Tan, Y. Wang, S. Zhu and J. Zhu, *Adv. Mater.*, , DOI:10.1002/adma.201604031.
- 41 Y. Wang, L. Zhang and P. Wang, *ACS Sustain. Chem. Eng.*, 2016, **4**, 1223–1230.
- 42 S. Zhuang, L. Zhou, W. Xu, N. Xu, X. Hu, X. Li, G. Lv, Q. Zheng, S. Zhu, Z. Wang and J. Zhu, *Adv. Sci.*, , DOI:10.1002/advs.201700497.
- 43 Y. Fu, G. Wang, X. Ming, X. Liu, B. Hou, T. Mei, J. Li, J. Wang and X. Wang, *Carbon N. Y.*, 2018, **130**, 250–256.
- 44 H. Li, Y. He, Y. Hu and X. Wang, *ACS Appl. Mater. Interfaces*, 2018, **10**, 9362–9368.
- 45 X. Liu, B. Hou, G. Wang, Z. Cui, X. Zhu and X. Wang, *J. Mater. Res.*, 2018, **33**, 674–684.
- 46 S. Liu, C. Huang, X. Luo and Z. Rao, *Appl. Therm. Eng.*, 2018, **142**, 566–572.
- 47 X. Li, X. Min, J. Li, N. Xu, P. Zhu, B. Zhu, S. Zhu and J. Zhu, *Joule*, 2018, **2**, 2477–2484.
- 48 Q. Zhang, X. Xiao, G. Wang, X. Ming, X. Liu, H. Wang, H. Yang, W. Xu and X. Wang, *J. Mater. Chem. A*, 2018, **6**, 17212–17219.
- 49 F. Tao, Y. Zhang, B. Wang, F. Zhang, X. Chang, R. Fan, L. Dong and Y. Yin, *Sol. Energy Mater. Sol. Cells*, 2018, **180**, 34–45.
- 50 W. Hao, K. Chiou, Y. Qiao, Y. Liu, C. Song, T. Deng and J. Huang, *Nanoscale*, 2018, **10**, 6306–6312.
- 51 P. Mu, Z. Zhang, W. Bai, J. He, H. Sun, Z. Zhu, W. Liang and A. Li, *Adv. Energy Mater.*, 2019, **9**, 1802158.
- 52 Y. Zhang, S. K. Ravi, J. V. Vaghasiya and S. C. Tan, *iScience*, 2018, **3**, 31–39.
- 53 M. Ye, K. Zhu, J. Gao, R. Chen and T. Zhang, *Water Supply*, 2019, 1–7.
- 54 Y. Luo, B. Fu, Q. Shen, W. Hao, J. Xu, M. Min, Y. Liu, S. An, C. Song, P. Tao, J. Wu, W. Shang and T. Deng, *ACS Appl. Mater. Interfaces*, 2019, **11**, 7584–7590.
- 55 X. Hu, W. Xu, L. Zhou, Y. Tan, Y. Wang, S. Zhu and J. Zhu, *Adv. Mater.*, 2017, **29**, 1604031.
- 56 Y. Li, T. Gao, Z. Yang, C. Chen, W. Luo, J. Song, E. Hitz, C. Jia, Y. Zhou, B. Liu, B. Yang and L. Hu, *Adv. Mater.*, 2017, **29**, 1–8.
- 57 X. Wang, Y. He, G. Cheng, L. Shi, X. Liu and J. Zhu, *Energy Convers. Manag.*, 2016, **130**, 176–183.
- 58 G. Wang, Y. Fu, X. Ma, W. Pi, D. Liu and X. Wang, *Carbon N. Y.*, 2017, **114**, 117–124.
- 59 G. Wang, Y. Fu, A. Guo, T. Mei, J. Wang, J. Li and X. Wang, *Chem. Mater.*, 2017, **29**, 5629–5635.
- 60 L. Shi, Y. Wang, L. Zhang and P. Wang, *J. Mater. Chem. A*, 2017, **5**, 16212–16219.

- 61 B. Huo, D. Jiang, X. Cao, H. Liang, Z. Liu, C. Li and J. Liu, *Carbon N. Y.*, 2019, **142**, 13–19.
- 62 M. Chen, Y. Wu, W. Song, Y. Mo, X. Lin, Q. He and B. Guo, *Nanoscale*, 2018, **10**, 6186–6193.
- 63 H. Li, Y. He, Z. Liu, B. Jiang and Y. Huang, *Energy*, 2017, **139**, 210–219.
- 64 J. Huang, Y. He, M. Chen, B. Jiang and Y. Huang, *Sol. Energy*, 2017, **155**, 1225–1232.
- 65 J. Huang, Y. He, Y. Hu and X. Wang, *Energy*, 2018, **165**, 1282–1291.
- 66 F. Tao, Y. Zhang, K. Yin, S. Cao, X. Chang, Y. Lei, D. Sheng Wang, R. Fan, L. Dong, Y. Yin and X. Chen, *ACS Appl. Mater. Interfaces*, 2018, **10**, 35154–35163.
- 67 G. Song, Y. Yuan, J. Liu, Q. Liu, W. Zhang, J. Fang, J. Gu, D. Ma and D. Zhang, *Adv. Sustain. Syst.*, 2019, **3**, 1900003.
- 68 X. Zhang, X. Wang, W. D. Wu, X. D. Chen and Z. Wu, *J. Mater. Chem. A*, 2019, **7**, 6963–6971.
- 69 X. Gao, H. Ren, J. Zhou, R. Du, C. Yin, R. Liu, H. Peng, L. Tong, Z. Liu and J. Zhang, *Chem. Mater.*, 2017, **29**, 5777–5781.
- 70 Y. Liu, S. Yu, R. Feng, A. Bernard, Y. Liu, Y. Zhang, H. Duan, W. Shang, P. Tao, C. Song and T. Deng, *Adv. Mater.*, 2015, **27**, 2768–2774.
- 71 L. Zhou, S. Zhuang, C. He, Y. Tan, Z. Wang and J. Zhu, *Nano Energy*, 2017, **32**, 195–200.
- 72 C. Liu, J. Huang, C.-E. Hsiung, Y. Tian, J. Wang, Y. Han and A. Fratalocchi, *Adv. Sustain. Syst.*, 2017, **1**, 1600013.
- 73 K. Bae, G. Kang, S. K. Cho, W. Park, K. Kim and W. J. Padilla, *Nat. Commun.*, 2015, **6**, 10103.
- 74 X. Wu, M. E. Robson, J. L. Phelps, J. S. Tan, B. Shao, G. Owens and H. Xu, *Nano Energy*, 2019, **56**, 708–715.
- 75 R. Chen, K. Zhu, Q. Gan, Y. Yu, T. Zhang, X. Liu, M. Ye and Y. Yin, *Mater. Chem. Front.*, 2017, **1**, 2620–2626.
- 76 F. Tao, Y. Zhang, S. Cao, K. Yin, X. Chang, Y. Lei, R. Fan, L. Dong, Y. Yin and X. Chen, *Mater. Today Energy*, 2018, **9**, 285–294.
- 77 N. Han, K. Liu, X. Zhang, M. Wang, P. Du, Z. Huang, D. Zhou, Q. Zhang, T. Gao, Y. Jia, L. Luo, J. Wang and X. Sun, *Sci. Bull.*, 2019, **64**, 391–399.
- 78 X. Wu, G. Y. Chen, W. Zhang, X. Liu and H. Xu, *Adv. Sustain. Syst.*, 2017, **1**, 1700046.
- 79 X. Luo, C. Huang, S. Liu and J. Zhong, *Int. J. Energy Res.*, 2018, **42**, 4830–4839.
- 80 K. K. Liu, Q. Jiang, S. Tadepalli, R. Raliya, P. Biswas, R. R. Naik and S. Singamaneni, *ACS Appl. Mater. Interfaces*, 2017, **9**, 7675–7681.
- 81 C. Chen, Y. Li, J. Song, Z. Yang, Y. Kuang, E. Hitz, C. Jia, A. Gong, F. Jiang, J. Y. Zhu, B. Yang, J. Xie and L. Hu, *Adv. Mater.*, 2017, **29**, 1–8.
- 82 G. Xue, K. Liu, Q. Chen, P. Yang, J. Li, T. Ding, J. Duan, B. Qi and J. Zhou, *ACS Appl. Mater. Interfaces*, 2017, **9**, 15052–15057.
- 83 C. Jia, Y. Li, Z. Yang, G. Chen, Y. Yao, F. Jiang, Y. Kuang, G. Pastel, H. Xie, B. Yang, S. Das and L. Hu, *Joule*, 2017, **1**, 588–599.
- 84 Z. J. Xia, H. C. Yang, Z. Chen, R. Z. Waldman, Y. Zhao, C. Zhang, S. N. Patel and S. B. Darling, *Adv. Mater. Interfaces*, 2019, **1900254**, 1–6.
- 85 Y. Wang, H. Liu, C. Chen, Y. Kuang, J. Song, H. Xie, C. Jia, S. Kronthal, X. Xu, S. He and L. Hu, *Adv. Sustain. Syst.*, 2019, **3**, 1800055.
- 86 J. Fang, J. Liu, J. Gu, Q. Liu, W. Zhang, H. Su and D. Zhang, *Chem. Mater.*, 2018, **30**, 6217–6221.
- 87 T. Chen, S. Wang, Z. Wu, X. Wang, J. Peng, B. Wu, J. Cui, X. Fang, Y. Xie and N. Zheng, *J. Mater. Chem. A*, 2018, **6**, 14571–14576.
- 88 J. Liu, Q. Liu, D. Ma, Y. Yuan, J. Yao, W. Zhang, H. Su, Y. Su, J. Gu and D. Zhang, *J. Mater. Chem. A*, 2019, **7**, 9034–9039.
- 89 N. Xu, X. Hu, W. Xu, X. Li, L. Zhou, S. Zhu and J. Zhu, *Adv. Mater.*, 2017, **29**, 1–5.
- 90 D. Hao, Y. Yang, B. Xu and Z. Cai, *Appl. Therm. Eng.*, 2018, **141**, 406–412.
- 91 C. Wang, Y. Wang, X. Song, M. Huang and H. Jiang, *Adv. Sustain. Syst.*, 2019, **3**, 1800108.
- 92 Z. Zhang, P. Mu, J. He, Z. Zhu, H. Sun, H. Wei, W. Liang and A. Li, *ChemSusChem*, 2019, **12**, 426–433.
- 93 L. An, P. Mu, W. Bai, Y. Fan, Z. Zhang, H.-X. Sun, Z.-Q. Zhu and W.-D. Liang, *J. Mater. Chem. A*, , DOI:10.1039/C8TA12243A.
- 94 W. Huang, G. Hu, C. Tian, X. Wang, J. Tu, Y. Cao and K. Zhang, *Sustain. Energy Fuels*, , DOI:10.1039/C9SE00163H.
- 95 X. Gao, H. Lan, S. Li, X. Lu, M. Zeng, X. Gao, Q. Wang, G. Zhou, J.-M. Liu, M. J. Naughton, K. Kempa and J. Gao, *Glob. Challenges*, 2018, **2**, 1800035.
- 96 P. Mu, W. Bai, Z. Zhang, J. He, H. Sun, Z. Zhu, W. Liang and A. Li, *J. Mater. Chem. A*, 2018, **6**, 18183–18190.
- 97 X. Yin, Y. Zhang, Q. Guo, X. Cai, J. Xiao, Z. Ding and J. Yang, *ACS Appl. Mater. Interfaces*, 2018, **10**, 10998–11007.
- 98 Z. Guo, G. Wang, X. Ming, T. Mei, J. Wang, J. Li, J. Qian and X. Wang, *ACS Appl. Mater. Interfaces*, 2018, **10**, 24583–24589.
- 99 G. Peng, H. Ding, S. W. Sharshir, X. Li, H. Liu, D. Ma, L. Wu, J. Zang, H. Liu, W. Yu, H. Xie and N. Yang, *Appl. Therm. Eng.*, 2018, **143**, 1079–1084.
- 100 P. Fan, H. Wu, M. Zhong, H. Zhang, B. Bai and G. Jin, *Nanoscale*, 2016, 14617–14624.
- 101 H. Liu, X. Zhang, Z. Hong, Z. Pu, Q. Yao, J. Shi, G. Yang, B. Mi, B. Yang, X. Liu, H. Jiang and X. Hu, *Nano Energy*, 2017, **42**, 115–121.
- 102 Y. Shi, R. Li, L. Shi, E. Ahmed, Y. Jin and P. Wang, *Adv. Sustain. Syst.*, 2018, **2**, 1870026.
- 103 X. Wu, L. Wu, J. Tan, G. Y. Chen, G. Owens and H. Xu, *J. Mater. Chem. A*, 2018, **6**, 12267–12274.
- 104 T. Gao, Y. Li, C. Chen, Z. Yang, Y. Kuang, C. Jia, J. Song, E. M. Hitz, B. Liu, H. Huang, J. Yu, B. Yang and L. Hu, *Small Methods*, 2019, **3**, 1800176.
- 105 J. Jia, W. Liang, H. Sun, Z. Zhu, C. Wang and A. Li, *Chem. Eng. J.*, 2019, 999–1006.
- 106 Q. Jiang, L. Tian, K.-K. Liu, S. Tadepalli, R. Raliya, P. Biswas, R. R. Naik and S. Singamaneni, *Adv. Mater.*, 2016, **28**, 9400–9407.
- 107 R. Li, L. Zhang, L. Shi and P. Wang, *ACS Nano*, 2017, **11**, 3752–3759.
- 108 Q. Jiang, H. Gholami Derami, D. Ghim, S. Cao, Y. S. Jun and

- S. Singamaneni, *J. Mater. Chem. A*, 2017, **5**, 18397–18402.
- 109 J. Fang, Q. Liu, W. Zhang, J. Gu, Y. Su, H. Su, C. Guo and D. Zhang, *J. Mater. Chem. A*, 2017, **5**, 17817–17821.
- 110 F. Zhang, Y. Li, X. Bai, S. Wang, B. Liang, G. Fu and Z. S. Wu, *J. Mater. Chem. A*, 2018, **6**, 23263–23269.
- 111 Z. Guo, X. Ming, G. Wang, B. Hou, X. Liu, T. Mei, J. Li, J. Wang and X. Wang, *Semicond. Sci. Technol.*, , DOI:10.1088/1361-6641/aaa323.
- 112 J. Wang, Z. Liu, X. Dong, C. E. Hsiung, Y. Zhu, L. Liu and Y. Han, *J. Mater. Chem. A*, 2017, **5**, 6860–6865.
- 113 C. Chen, Y. Kuang and L. Hu, *Joule*, 2019, **3**, 683–718.
- 114 H. Jin, G. Lin, L. Bai, A. Zeiny and D. Wen, *Nano Energy*, 2016, **28**, 397–406.
- 115 L. Zhou, Y. Tan, D. Ji, B. Zhu, P. Zhang, J. Xu, Q. Gan, Z. Yu and J. Zhu, *Sci. Adv.*, 2016, **2**, e1501227.
- 116 L. Zhou, S. Zhuang, C. He, Y. Tan, Z. Wang and J. Zhu, *Nano Energy*, 2017, **32**, 195–200.
- 117 M. Zhu, Y. Li, G. Chen, F. Jiang, Z. Yang, X. Luo, Y. Wang, S. D. Lacey, J. Dai, C. Wang, C. Jia, J. Wan, Y. Yao, A. Gong, B. Yang, Z. Yu, S. Das and L. Hu, *Adv. Mater.*, 2017, **29**, 1–9.
- 118 S. Zhuang, L. Zhou, W. Xu, N. Xu, X. Hu, X. Li, G. Lv, Q. Zheng, S. Zhu, Z. Wang and J. Zhu, *Adv. Sci.*, , DOI:10.1002/advs.201700497.
- 119 X. Huang, Y. H. Yu, O. L. De Llargo, S. M. Marquez and Z. Cheng, *RSC Adv.*, 2017, **7**, 9495–9499.
- 120 L. Zhang, B. Tang, J. Wu, R. Li and P. Wang, *Adv. Mater.*, 2015, **27**, 4889–4894.
- 121 J. Huang and R. B. Kaner, *Nat. Mater.*, 2004, **3**, 783–786.
- 122 M. Gao, L. Zhu, C. K. Peh and G. W. Ho, *Energy Environ. Sci.*, 2019, **12**, 841–864.
- 123 J. Wang, Y. Li, L. Deng, N. Wei, Y. Weng, S. Dong, D. Qi, J. Qiu, X. Chen and T. Wu, *Adv. Mater.*, 2016, 1–6.
- 124 G. Zhu, J. Xu, W. Zhao and F. Huang, *ACS Appl. Mater. Interfaces*, 2016, **8**, 31716–31721.
- 125 R. Chen, Z. Wu, T. Zhang, T. Yu and M. Ye, *RSC Adv.*, 2017, **7**, 19849–19855.
- 126 Y. Shi, R. Li, Y. Jin, S. Zhuo, L. Shi, J. Chang, S. Hong, K. C. Ng and P. Wang, *Joule*, 2018, **2**, 1171–1186.
- 127 D. Ding, W. Huang, C. Song, M. Yan, C. Guo and S. Liu, *Chem. Commun.*, 2017, **53**, 6744–6747.
- 128 Z. Hua, B. Li, L. Li, X. Yin, K. Chen and W. Wang, *J. Phys. Chem. C*, 2017, **121**, 60–69.
- 129 C. Song, T. Li, W. Guo, Y. Gao, C. Yang, Q. Zhang, D. An, W. Huang, M. Yan and C. Guo, *New J. Chem.*, 2018, **42**, 3175–3179.
- 130 T. Zhang, S. V. Boriskina, G. Chen, G. Ni, G. Li, H. Li and W. Yang, *Nat. Energy*, , DOI:10.1038/nenergy.2016.126.
- 131 Y. Shao, Z. Jiang, Y. Zhang, T. Wang, P. Zhao, Z. Zhang, J. Yuan and H. Wang, *ACS Nano*, 2018, **12**, 11704–11710.
- 132 H. Li, Y. He, Z. Liu, Y. Huang and B. Jiang, *Appl. Therm. Eng.*, 2017, **121**, 617–627.
- 133 H. Song, Y. Liu, Z. Liu, M. H. Singer, C. Li, A. R. Cheney, D. Ji, L. Zhou, N. Zhang, X. Zeng, Z. Bei, Z. Yu, S. Jiang and Q. Gan, *Adv. Sci.*, , DOI:10.1002/advs.201800222.
- 134 M. Gao, C. K. Peh, H. T. Phan, L. Zhu and G. W. Ho, *Adv. Energy Mater.*, 2018, **8**, 1–9.
- 135 X. Ming, A. Guo, G. Wang and X. Wang, *Sol. Energy Mater. Sol. Cells*, 2018, **185**, 333–341.
- 136 P. Ren and X. Yang, *Sol. RRL*, 2018, **2**, 1700233.
- 137 M. M. Ghafurian, H. Niazmand, E. Ebrahimnia-Bajestan and H. Elhami Nik, *J. Therm. Anal. Calorim.*, 2019, **135**, 1443–1449.
- 138 T. Wu, H. Li, M. Xie, S. Shen, W. Wang, M. Zhao, X. Mo and Y. Xia, *Mater. Today Energy*, 2019, **12**, 129–135.
- 139 F. M. Canbazoglu, B. Fan, A. Kargar, K. Vemuri and P. R. Bandaru, *AIP Adv.*, , DOI:10.1063/1.4961945.
- 140 L. Chen, D. Li, Y. Wang and C. Duan, *Nanoscale*, , DOI:10.1039/c8nr09080g.
- 141 C. Xue, S. Hu, Q. Chang, N. Li, Y. Wang, W. Liu and J. Yang, *J. Mater. Sci.*, 2018, **53**, 9742–9754.
- 142 Q. Hou, C. Xue, N. Li, H. Wang, Q. Chang, H. Liu, J. Yang and S. Hu, *Carbon N. Y.*, 2019, **149**, 556–563.
- 143 Y. Ito, Y. Tanabe, J. Han, T. Fujita, K. Tanigaki and M. Chen, *Adv. Mater.*, 2015, **27**, 4302–4307.
- 144 J. Yang, Y. Pang, W. Huang, S. K. Shaw, J. Schiffbauer, M. A. Pillers, X. Mu, S. Luo, T. Zhang, Y. Huang, G. Li, S. Ptasinska, M. Lieberman and T. Luo, *ACS Nano*, 2017, **11**, 5510–5518.
- 145 C. Zhang, C. Yan, Z. Xue, W. Yu, Y. Xie and T. Wang, *Small*, 2016, **12**, 5320–5328.
- 146 S. Ishii, R. P. Sugavaneshwar, K. Chen, T. D. Dao and T. Nagao, *Opt. Mater. Express*, 2016, **6**, 640.
- 147 K. Watkins, *Human Development Report 2006 - Beyond scarcity: Power, poverty and the global water crisis*, 2006, vol. 28.
- 148 Organización de las Naciones Unidas, *Un Water*, 2005, **24**, 28–29.
- 149 Y. Liu, X. Wang and H. Wu, *Chem. Eng. J.*, 2017, **309**, 787–794.
- 150 M. Fujiwara, *Desalination*, 2017, **404**, 79–86.
- 151 Y. Liu, J. Lou, M. Ni, C. Song, J. Wu, N. P. Dasgupta, P. Tao, W. Shang and T. Deng, *ACS Appl. Mater. Interfaces*, 2016, **8**, 772–779.
- 152 F. Zhao, X. Zhou, Y. Shi, X. Qian, M. Alexander, X. Zhao, S. Mendez, R. Yang, L. Qu and G. Yu, *Nat. Nanotechnol.*, 2018, **13**, 489–495.
- 153 L. Zhou, Y. Tan, J. Wang, W. Xu, Y. Yuan, W. Cai, S. Zhu and J. Zhu, *Nat. Photonics*, 2016, **10**, 1–13.
- 154 Y. Xia, Q. Hou, H. Jubaer, Y. Li, Y. Kang, S. Yuan, H. Liu, M. W. Woo, L. Zhang, L. Gao, H. Wang and X. Zhang, *Energy Environ. Sci.*, , DOI:10.1039/c9ee00692c.
- 155 X. Zhou, F. Zhao, Y. Guo, Y. Zhang and G. Yu, *Energy Environ. Sci.*, 2018, **11**, 1985–1992.
- 156 G. W. Ni, S. H. Zandavi, S. M. Javid, S. V. Boriskina, T. A. Cooper and G. Chen, *Energy Environ. Sci.*, , DOI:10.1039/C8EE00220G.
- 157 E. Chiavazzo, M. Morciano, F. Viglino, M. Fasano and P. Asinari, *Nat. Sustain.*, 2017, **1**, 763–772.
- 158 X. Lin, J. Chen, Z. Yuan, M. Yang, G. Chen, D. Yu, M. Zhang, W. Hong and X. Chen, *J. Mater. Chem. A*, 2018, **6**, 4642–4648.
- 159 Y. Wang, C. Wang, X. Song, M. Huang, S. K. Megarajan, S. F. Shaikat and H. Jiang, *J. Mater. Chem. A*, 2018, **6**, 9874–9881.
- 160 Y. Jin, J. Chang, Y. Shi, L. Shi, S. Hong and P. Wang, *J. Mater.*

- Chem. A*, 2018, **6**, 7942–7949.
- 161 L. Cui, P. Zhang, Y. Xiao, Y. Liang, H. Liang, Z. Cheng and L. Qu, *Adv. Mater.*, 2018, **30**, 1–6.
- 162 P. F. Liu, L. Miao, Z. Deng, J. Zhou, H. Su, L. Sun, S. Tanemura, W. Cao, F. Jiang and L. D. Zhao, *Mater. Today Energy*, 2018, **8**, 166–173.
- 163 Y. Yang, X. Yang, L. Fu, M. Zou, A. Cao, Y. Du, Q. Yuan and C.-H. Yan, *ACS Energy Lett.*, 2018, **3**, 1165–1171.
- 164 Z. Deng, P.-F. Liu, J. Zhou, L. Miao, Y. Peng, H. Su, P. Wang, X. Wang, W. Cao, F. Jiang, L. Sun and S. Tanemura, *Sol. RRL*, 2018, **2**, 1800073.
- 165 G. Li, W. C. Law and K. C. Chan, *Green Chem.*, 2018, **20**, 3689–3695.
- 166 J. Zhao, Y. Yang, C. Yang, Y. Tian, Y. Han, J. Liu, X. Yin and W. Que, *J. Mater. Chem. A*, 2018, **6**, 16196–16204.
- 167 M. Shang, N. Li, S. Zhang, T. Zhao, C. Zhang, C. Liu, H. Li and Z. Wang, *ACS Appl. Energy Mater.*, 2018, **1**, 56–61.
- 168 Y. Chang, Z. Wang, Y. E. Shi, X. Ma, L. Ma, Y. Zhang and J. Zhan, *J. Mater. Chem. A*, 2018, **6**, 10939–10946.
- 169 W. Chen, C. Zou, X. Li and H. Liang, *Desalination*, 2019, **451**, 92–101.
- 170 P. Zhang, Q. Liao, H. Yao, H. Cheng, Y. Huang, C. Yang, L. Jiang and L. Qu, *J. Mater. Chem. A*, 2018, **6**, 15303–15309.
- 171 Y. Shi, C. Zhang, R. Li, S. Zhuo, Y. Jin, L. Shi, S. Hong, J. Chang, C. Ong and P. Wang, *Environ. Sci. Technol.*, 2018.
- 172 C. Mu, Y. Song, K. Deng, S. Lin, Y. Bi, F. Scarpa and D. Crouse, *Adv. Sustain. Syst.*, 2017, **1**, 1700064.
- 173 G. Xue, Q. Chen, S. Lin, J. Duan, P. Yang, K. Liu, J. Li and J. Zhou, *Glob. Challenges*, 2018, **2**, 1800001.
- 174 J. Xu, F. Xu, M. Qian, Z. Li, P. Sun, Z. Hong and F. Huang, *Nano Energy*, 2018, **53**, 425–431.
- 175 H. Liu, C. Chen, H. Wen, R. Guo, N. A. Williams, B. Wang, F. Chen and L. Hu, *J. Mater. Chem. A*, 2018, **6**, 18839–18846.
- 176 F. S. Awad, H. D. Kiriarachchi, K. M. Abouzeid, Ü. Özgür and M. S. El-Shall, *ACS Appl. Energy Mater.*, 2018, **1**, 976–985.
- 177 M. Zhu, J. Yu, C. Ma, C. Zhang, D. Wu and H. Zhu, *Sol. Energy Mater. Sol. Cells*, 2019, **191**, 83–90.
- 178 H. D. Kiriarachchi, F. S. Awad, A. A. Hassan, J. A. Bobb, A. Lin and M. S. El-Shall, *Nanoscale*, 2018, **10**, 18531–18539.
- 179 L. Zhu, L. Sun, H. Zhang, D. Yu, H. Aslan, J. Zhao, Z. Li, M. Yu, F. Besenbacher and Y. Sun, *Nano Energy*, 2019, **57**, 842–850.
- 180 L. Shi, Y. Shi, R. Li, J. Chang, N. Zaouri, E. Ahmed, Y. Jin, C. Zhang, S. Zhuo and P. Wang, *ACS Sustain. Chem. Eng.*, 2018, **6**, 8192–8200.
- 181 S. Ma, W. Qarony, M. I. Hossain, C. T. Yip and Y. H. Tsang, *Sol. Energy Mater. Sol. Cells*, 2019, **196**, 36–42.
- 182 Q. Ma, P. Yin, M. Zhao, Z. Luo, Y. Huang, Q. He, Y. Yu, Z. Liu, Z. Hu, B. Chen and H. Zhang, *Adv. Mater.*, 2019, **31**, 1–7.
- 183 X. Song, H. Song, N. Xu, H. Yang, L. Zhou, L. Yu, J. Zhu, J. Xu and K. Chen, *J. Mater. Chem. A*, 2018, **6**, 22976–22986.
- 184 F. (Frank) Gong, H. Li, W. Wang, J. Huang, D. (David) Xia, J. Liao, M. Wu and D. V. Papavassiliou, *Nano Energy*, 2019, **58**, 322–330.
- 185 Z. Xiong, Y. Zhu, D. Qin, F. Chen and R. Yang, *Small*, 2018, **14**, 1803387.
- 186 H. Su, J. Zhou, L. Miao, J. Shi, Y. Gu, P. Wang, Y. Tian, X. Mu, A. Wei, L. Huang, S. Chen and Z. Deng, *Sustain. Mater. Technol.*, 2019, **20**, e00095.
- 187 P. Qiao, J. Wu, H. Li, Y. Xu, L. Ren, K. Lin and W. Zhou, *ACS Appl. Mater. Interfaces*, 2019, **11**, 7066–7073.
- 188 G. G. Jang, J. W. Klett, J. McFarlane, A. Ilevlev, K. Xiao, J. K. Keum, M. Yoon, P. Im, M. Z. Hu and J. E. Parks, *Glob. Challenges*, 2019, **1900003**, 1900003.
- 189 Z. Li, C. Wang, T. Lei, H. Ma, J. Su, S. Ling and W. Wang, *Adv. Sustain. Syst.*, 2019, **3**, 1800144.
- 190 Q. Lu, Y. Yang, J. Feng and X. Wang, *Sol. RRL*, 2019, **3**, 1800277.
- 191 Q. Zhang, H. Yang, X. Xiao, H. Wang, L. Yan, Z. Shi, Y. Chen, W. Xu and X. Wang, *J. Mater. Chem. A*, , DOI:10.1039/c9ta03045j.
- 192 P. Xiao, J. He, Y. Liang, C. Zhang, J. Gu, J. Zhang, Y. Huang, S.-W. Kuo and T. Chen, *Sol. RRL*, 2019, 1900004.
- 193 R. Chen, X. Wang, Q. Gan, T. Zhang, K. Zhu and M. Ye, *J. Mater. Chem. A*, 2019, **7**, 11177–11185.
- 194 A. Celzard, A. Pasc, S. Schaefer, K. Mandel, T. Ballweg, S. Li, G. Medjahdi, V. Nicolas and V. Fierro, *Carbon N. Y.*, 2019, **146**, 232–247.
- 195 H. Kou, Z. Liu, B. Zhu, D. K. Macharia, S. Ahmed, B. Wu, M. Zhu, X. Liu and Z. Chen, *Desalination*, 2019, **462**, 29–38.
- 196 X. Han, W. Wang, K. Zuo, L. Chen, L. Yuan, J. Liang, Q. Li, P. M. Ajayan, Y. Zhao and J. Lou, *Nano Energy*, 2019, **60**, 567–575.
- 197 H. M. Wilson, S. Rahman A.R., A. E. Parab and N. Jha, *Desalination*, 2019, **456**, 85–96.
- 198 Y. Liu, Z. Liu, Q. Huang, X. Liang, X. Zhou, H. Fu, Q. Wu, J. Zhang and W. Xie, *J. Mater. Chem. A*, 2019, **7**, 2581–2588.
- 199 Q. Fang, T. Li, Z. Chen, H. Lin, P. Wang and F. Liu, *ACS Appl. Mater. Interfaces*, 2019, **11**, 10672–10679.
- 200 Y. Kuang, C. Chen, S. He, E. M. Hitz, Y. Wang, W. Gan, R. Mi and L. Hu, *Adv. Mater.*, 2019, **31**, 1900498.
- 201 X. Feng, J. Zhao, D. Sun, L. Shanmugam, J.-K. Kim and J. Yang, *J. Mater. Chem. A*, 2019, **7**, 4400–4407.
- 202 D. D. Qin, Y. J. Zhu, F. F. Chen, R. L. Yang and Z. C. Xiong, *Self-floating aerogel composed of carbon nanotubes and ultralong hydroxyapatite nanowires for highly efficient solar energy-assisted water purification*, Elsevier Ltd, 2019, vol. 150.
- 203 P. Qiu, F. Liu, C. Xu, H. Chen, F. Jiang, Y. Li and Z. Guo, *J. Mater. Chem. A*, , DOI:10.1039/c9ta00041k.
- 204 X. Ma, W. Fang, Y. Guo, Z. Li, D. Chen, W. Ying, Z. Xu, C. Gao and X. Peng, *Small*, , DOI:10.1002/smll.201900354.
- 205 C. Li, D. Jiang, B. Huo, M. Ding, C. Huang, D. Jia, H. Li, C. Y. Liu and J. Liu, *Nano Energy*, 2019, **60**, 841–849.
- 206 X. Wang, Q. Liu, S. Wu, B. Xu and H. Xu, *Adv. Mater.*, 2019, **31**, 1807716.
- 207 Y. Guo, F. Zhao, X. Zhou, Z. Chen and G. Yu, *Nano Lett.*, 2019, **19**, 2530–2536.
- 208 P. Zhang, J. Li, L. Lv, Y. Zhao and L. Qu, *ACS Nano*, 2017, **11**, 5087–5093.
- 209 H. Ren, M. Tang, B. Guan, K. Wang, J. Yang, F. Wang, M. Wang, J. Shan, Z. Chen, D. Wei, H. Peng and Z. Liu, *Adv. Mater.*, 2017, **29**, 1–7.
- 210 Z. Liu, H. Song, D. Ji, C. Li, A. Cheney, Y. Liu, N. Zhang, X.

- Zeng, B. Chen, J. Gao, Y. Li, X. Liu, D. Aga, S. Jiang, Z. Yu and Q. Gan, *Glob. Challenges*, 2017, **201600003**, 1600003.
- 211 P. D. Dongare, A. Alabastri, S. Pedersen, K. R. Zodrow, N. J. Hogan, O. Neumann, J. Wu, T. Wang, A. Deshmukh, M. Elimelech, Q. Li, P. Nordlander and N. J. Halas, *Proc. Natl. Acad. Sci. U. S. A.*, 2017, **114**, 6936–6941.
- 212 X. Wang, G. Ou, N. Wang and H. Wu, *ACS Appl. Mater. Interfaces*, 2016, **8**, 9194–9199.
- 213 Y. Yang, R. Zhao, T. Zhang, K. Zhao, P. Xiao, Y. Ma, P. M. Ajayan, G. Shi and Y. Chen, *ACS Nano*, 2018, **12**, 829–835.
- 214 S. M. Sajadi, P. Irajizad, V. Kashyap, N. Farokhnia and H. Ghasemi, *Appl. Phys. Lett.*, 2017, **111**, 021605.
- 215 Y. Li, T. Gao, Z. Yang, C. Chen, Y. Kuang, J. Song, C. Jia, E. M. Hitz, B. Yang and L. Hu, *Nano Energy*, 2017, **41**, 201–209.
- 216 Z. Wang, Q. Ye, X. Liang, J. Xu, C. Chang, C. Song, W. Shang, J. Wu, P. Tao and T. Deng, *J. Mater. Chem. A*, 2017, **5**, 16359–16368.
- 217 Z. Yin, H. Wang, M. Jian, Y. Li, K. Xia, M. Zhang, C. Wang, Q. Wang, M. Ma, Q. Zheng and Y. Zhang, *ACS Appl. Mater. Interfaces*, 2017, **9**, 28596–28603.
- 218 Q. Chen, Z. Pei, Y. Xu, Z. Li, Y. Yang, Y. Wei and Y. Ji, *Chem. Sci.*, 2018, **9**, 623–628.
- 219 X. Wang, Y. He, X. Liu, G. Cheng and J. Zhu, *Appl. Energy*, 2017, **195**, 414–425.
- 220 M. Zhu, Y. Li, F. Chen, X. Zhu, J. Dai, Y. Li, Z. Yang, X. Yan, J. Song, Y. Wang, E. Hitz, W. Luo, M. Lu, B. Yang and L. Hu, *Adv. Energy Mater.*, 2018, **8**, 1–7.
- 221 W. Xu, X. Hu, S. Zhuang, Y. Wang, X. Li, L. Zhou, S. Zhu and J. Zhu, *Adv. Energy Mater.*, 2018, **8**, 1–7.
- 222 X. Yang, Y. Yang, L. Fu, M. Zou, Z. Li, A. Cao and Q. Yuan, *Adv. Funct. Mater.*, 2018, **28**, 1–9.
- 223 L. Yi, S. Ci, S. Luo, P. Shao, Y. Hou and Z. Wen, *Nano Energy*, 2017, **41**, 600–608.
- 224 Y. Shi, R. Li, Y. Jin, S. Zhuo, L. Shi, J. Chang, S. Hong, K. C. Ng and P. Wang, *Joule*, 2018, **2**, 1171–1186.
- 225 Z. Liu, Z. Yang, X. Huang, C. Xuan, J. Xie, H. Fu, Q. Wu, J. Zhang, X. Zhou and Y. Liu, *J. Mater. Chem. A*, 2017, **5**, 20044–20052.
- 226 Y. Yang, W. Que, J. Zhao, Y. Han, M. Ju and X. Yin, *Chem. Eng. J.*, 2019, **373**, 955–962.
- 227 J. Zhao, Y. Yang, C. Yang, Y. Tian, Y. Han, J. Liu, X. Yin and W. Que, *J. Mater. Chem. A*, 2018, **6**, 16196–16204.
- 228 O. Neumann, C. Feronti, A. D. Neumann, A. Dong, K. Schell, B. Lu, E. Kim, M. Quinn, S. Thompson, N. Grady, P. Nordlander, M. Oden and N. J. Halas, *Proc. Natl. Acad. Sci. U. S. A.*, 2013, **110**, 11677–81.
- 229 P. Yang, K. Liu, Q. Chen, J. Li, J. Duan, G. Xue, Z. Xu, W. Xie and J. Zhou, *Energy Environ. Sci.*, 2017, **10**, 1923–1927.
- 230 X. Q. Wang, C. F. Tan, K. H. Chan, K. Xu, M. Hong, S. W. Kim and G. W. Ho, *ACS Nano*, 2017, **11**, 10568–10574.
- 231 C. Chen, L. Zhou, J. Yu, Y. Wang, S. Nie, S. Zhu and J. Zhu, *Nano Energy*, 2018, **51**, 451–456.
- 232 V. Kashyap, R. Medhi, P. Irajizad, P. Jafari, M. Nazari, A. Masoudi, M. D. Marquez, T. R. Lee and H. Ghasemi, *Sustain. Energy Fuels*, 2019, **3**, 272–279.
- 233 L. Shi, Y. He, X. Wang and Y. Hu, *Energy Convers. Manag.*, 2018, **171**, 272–278.
- M. W. Higgins, A. R. Shakeel Rahmaan, R. R. Devarapalli, M. V. Shelke and N. Jha, *Sol. Energy*, 2018, **159**, 800–810.
- 235 X. Wang, Y. He and X. Liu, *Energy Convers. Manag.*, 2018, **173**, 158–166.
- 236 X. Xu, P. Wang, J. Zhang, Y. Jin, C. Li and M. Wang, *Nano Res.*, 2017, **11**, 3854–3863.
- 237 D. Ghim, Q. Jiang, S. S. Cao, S. Singamaneni and Y. S. Jun, *Nano Energy*, 2018, **53**, 949–957.
- 238 Q. Gan, T. Zhang, R. Chen, X. Wang and M. Ye, *ACS Sustain. Chem. Eng.*, 2019, **7**, 3925–3932.
- 239 H. Geng, Q. Xu, M. Wu, H. Ma, P. Zhang, T. Gao, L. Qu, T. Ma and C. Li, *Nat. Commun.*, 2019, **10**, 1–10.
- 240 J. Lou, Y. Liu, Z. Wang, D. Zhao, C. Song, J. Wu, N. Dasgupta, W. Zhang, D. Zhang, P. Tao, W. Shang and T. Deng, *ACS Appl. Mater. Interfaces*, 2016, **8**, 14628–14636.
- 241 S. Ma, C. P. Chiu, Y. Zhu, C. Y. Tang, H. Long, W. Qarony, X. Zhao, X. Zhang, W. H. Lo and Y. H. Tsang, *Appl. Energy*, 2017, **206**, 63–69.
- 242 Y. Yang, H. Zhao, Z. Yin, J. Zhao, X. Yin, N. Li, D. Yin, Y. Li, B. Lei, Y. Du and W. Que, *Mater. Horizons*, 2018, **5**, 1143–1150.
- 243 Y. Zhang, D. Zhao, F. Yu, C. Yang, J. Lou, Y. Liu, Y. Chen, Z. Wang, P. Tao, W. Shang, J. Wu, C. Song and T. Deng, *Nanoscale*, 2017, **9**, 19384–19389.
- 244 J. Li, M. Du, G. Lv, L. Zhou, X. Li, L. Bertoluzzi, C. Liu, S. Zhu and J. Zhu, *Adv. Mater.*, 2018, **30**, 1–7.
- 245 C. Chang, P. Tao, J. Xu, B. Fu, C. Song, J. Wu, W. Shang and T. Deng, *ACS Appl. Mater. Interfaces*, DOI:10.1021/acsami.9b04535.
- 246 X. Zhang, W. Gao, X. Su, F. Wang, B. Liu, J. J. Wang, H. Liu and Y. Sang, *Nano Energy*, 2018, **48**, 481–488.
- 247 Z. Lin, J. Li, Z. Zheng, L. Li, L. Yu, C. Wang and G. Yang, *Adv. Energy Mater.*, 2016, **6**, 1–10.
- 248 J. Chang, Y. Shi, M. Wu, R. Li, L. Shi, Y. Jin, W. Qing, C. Tang and P. Wang, *J. Mater. Chem. A*, 2018, **6**, 9192–9199.
- 249 H. R. Liu, A. Raza, A. Aili, J. Y. Lu, A. Alghaferi and T. J. Zhang, *Sci. Rep.*, 2016, **6**, 1–10.
- 250 B. Hou, D. Kong, J. Qian, Y. Yu, Z. Cui, X. Liu, J. Wang, T. Mei, J. Li and X. Wang, *Carbon N. Y.*, 2018, **140**, 488–493.
- 251 X. Li, W. Xu, M. Tang, L. Zhou, B. Zhu, S. Zhu and J. Zhu, *Proc. Natl. Acad. Sci.*, 2016, **113**, 13953–13958.
- 252 G. W. Ni, S. H. Zandavi, S. M. Javid, S. V. Boriskina, T. A. Cooper and G. Chen, *Energy Environ. Sci.*, DOI:10.1039/C8EE00220G.